Chapter 3

Band gap Narrowing of $xPbTiO_3$-$(1-x)Bi(Ni_{2/3}Nb_{1/3})O_3$ ceramics, and Photo-voltaic effect in its PLD grown thin films

3.1 Introduction

Recently, there is enormous interest in ferroelectric photovoltaic (PV) materials, especially the multiferroics with higher polarization value and lower band gap. Over the past few years, vigorous efforts have been devoted to ferroelectric materials for application in photovoltaic devices due to their outstanding advantages, such as, large photovoltage, polarization-dependent photocurrent, single device structure and cheaper constitutive materials. As discussed in section 1.2 of Chapter-1, Perovskite-type Multiferroic materials are gaining widespread popularity in photovoltaic applications due to their capability to generate bulk photovoltage and ability to improve the mobility of charge carriers [S. Y. Yang et al. (2010)]. Ferroelectric photovoltaic effect is reported in many perovskite oxide materials, such as, $LiNbO_3$, $BaTiO_3$, $PbTiO_3$, and $BiFeO_3$ [A. M. Glass et al. (1974); J. W. Bennettet al. (2008); T. Choi et al. (2009)].

Perovskite $PbTiO_3$ is the most studied ferroelectric compound with a high curie temperature (490°C), thus being a good candidate for ferroelectric devices. The $PbTiO_3$ have high spontaneous polarization and have shown anomalous photovoltaic effect as discussed in section 1.8.2 of chapter-1 [V. M. Fridkin et al. (1978)]. However, due to wide band gap of material, the photocurrent is very low limiting its practical applications. Therefore, it is very necessary to reduce the band gap of $PbTiO_3$ to get high photocurrent for large scale applications. In an early study, it is reported that cationic substitution at the B-site of Pb-based ABO_3 perovskites can reduce the band gap [J. W. Bennet et al. (2008)].

W. Zhou et al. (2011) have reported a reduced band gap (~2.42 eV) of $PbTiO_3$ after Ni doping. The Ni doped thin films show reduced band gap (~ 2.86 eV) and increased remnant polarization [C. W. Zhao et al. (2017)]. The research works on

$xPbTiO_3$-(1-x)$Bi(Ni_{2/3}Nb_{1/3})O_3$ (PT-BNN) ceramics show that the composition (x= 0.65) near the morphotropic phase boundary have improved remnant polarization [S. Zhang et al. (2005)], which makes this solid solution to be excellent candidate for ferroelectric photovoltaic devices. S. Zhang et al. have reported MPB region (x = 0.625-0.65) in PT-BNN [S. Zhang et al. (2005)] and H. Liu et al. have reported bulk photovoltaic effect for 0.65PT-BNN ceramic pellets [H. Liu et al. (2015)] with an band gap of 2.5eV (Indirect band gap). However, in these studies, the PV effect is reported in polycrystalline thick ceramics pellets of PT-BNN and effect of thickness is neglected. The ceramic pellets with Pt/PT-BNN/Ag device structure show high photovoltage but very low photocurrent. The low photocurrent is due to high thickness of absorbing layer which causes charge recombination. Therefore, to design solar cells with high photocurrent, it is desirable to lower the band gap of photoactive layer and use it in the thin film form. Such issues can be solved by further reducing the band gap of PT-BNN ceramics by further doping and depositing its thin film.

This chapter presents the results of our investigation on the optical band gap of $xPbTiO_3$-(1-x)$Bi(Ni_{2/3}Nb_{1/3})O_3$ solid solution in the wider composition range ($0.87 \leq x \leq 0.50$).In order to get lower band gap with suitable ferroelectricity, we used Bi^{3+} and Ni^{2+} doping to design a better perovskite ferroelectric solid solution $xPbTiO_3$-(1-x)$Bi(Ni_{2/3}Nb_{1/3})O_3$. Here, Ni^{2+} acts as band gap reducing element while Bi^{3+} will maintain the ferroelectric nature due to its $6s^2$ lone pair electron configuration [P. Baettig et al. (2005)]. The perovskite ferroelectric solid solution $xPbTiO_3$-(1-x)$Bi(Ni_{2/3}Nb_{1/3})O_3$[xPT-(1-x)BNN]were synthesized by solid state reaction method and its physical properties were investigated with varying the BNN doping. In this study, we also demonstrate the effect of Ni/Nb and Ni/Co stoichiometric ratio change on optical band gap of xPT-(1-x)BNN. We have also investigated the band gap and

ferroelectric properties of different compositions of the multiferroic composites of 0.65PT-BNN with magnetic phase $Ni_{0.65}Zn_{0.35}Fe_2O_4$ and $Co_{0.5}Zn_{0.5}Fe_2O_4$. Further, we present the result of our investigation to assess the feasibility of PT-BNN thin films deposition by pulsed laser deposition (PLD). We have demonstrated for the first time the thin film growth of PT-BNN and its photovoltaic behaviour.

3.2 Experimental

Various compositions of $xPbTiO_3$-$(1-x)Bi(Ni_{2/3}Nb_{1/3})O_3$ solid solution (x= 0.87, 0.77, 0.70, 0.67, 0.66, 0.65, 0.64, 0.63, 0.625, 0.62, 0.60, 0.55 and 0.50) were synthesized by conventional solid state route of 'ceramic preparation'. The details of synthesis route and sintering optimization steps of ceramic pellets are presented in chapter-2. Powder X-ray diffraction (XRD) measurements were performed at room temperature from 20^o to 120^o using powder diffractometer (RIGAKU MINIFLEX 600) using Cu-K_α radiation. The ferroelectric polarization as a function of external field was examined by ferroelectric tester based on standard Sawyer-Tower circuit (Radiant Technologies, USA) in frequency range from 1 to 1000 Hz at room temperature. The Ultra-violet-visible absorbance spectra recorded at room temperature using Spectrophotometer (Horiba Jobin Yvon) and the optical band gap was calculated by Tauc equation. In order to study photovoltaic phenomenon in PT-BNN, thin films are deposited on LSMO coated STO substrates by PLD with a KrF excimer laser. The surface morphology and ferroelectric switching behavior of PT-BNN films at nanoscale was visualized by using combination of atomic force microscopy (AFM) and piezoresponse force microscopy (PFM). The current –voltage (I-V) measurement of as prepared device is measured using Keithley 6517B Electrometer.

3.3 Results and Discussion

3.3.1 Structural Investigation

Room temperature XRD patterns for $xPbTiO_3$-(1-x)$Bi(Ni_{2/3}Nb_{1/3})O_3$solid solution in the composition range ($0.50 \leq x \leq 0.87$) are shown in Fig. 3.1. These XRD data shows that all the compositions of as synthesized PT-BNN ceramics have perovskite structure without any secondary phase. It is evident from Fig. 3.1 (a) that the XRD peaks for samples with compositions $0.65 < x \leq 0.87$ are well indexed using tetragonal structure in *P*4*mm* space group similar to $PbTiO_3$. The large angular separation between the two XRD peaks (002) and (200) shown in Fig.3, demonstrates the high tetragonality and consequently larger polarization for these compositions of PT-BNN. The characteristic (002) and (200) doublet splitting of the tetragonal structure is observed in samples with composition ($0.65 < x \leq 0.87$). With increase in BNN concentration, the angular separation between (002) and (200) peaks reduces and no detectable tetragonal splitting is observed for [100] and [110] peaks for samples with composition $x < 0.62$. The XRD pattern of these compositions can be indexed with cubic structure in *Pm*3*m* space group and the true structure may be rhombohedral/pseudo-cubic for the compositions with $x < 0.62$. In the compositions range $0.625 \leq x \leq 0.65$, mixed character of (200) peak is seen due to presence of both the tetragonal and rhombohedral/pseudo-cubic phases and this region is termed as the morphotropic phase boundary (MPB) region for PT-BNN.

In MPB region, the (200) XRD profile has two peaks of tetragonal (002) and (020) and one cubic (200) peak in between them as shown in Fig. 3.1(b), making the composite profile a broad asymmetric peak. The structure of compositions in the range is neither rhombohedral nor tetragonal but the coexistence of both these phases. The observation of MPB region in PT-BNN ceramics for compositions ($0.625 \leq x \leq 0.65$)

may be attributed to the disruption of the Ti-O orbital hybridization balance which caused by the substitution of Ti^{4+}(0.74Å) by the off-valent Ni^{2+}(0.69Å) and Nb^{4+} ions (0.74Å) [W. Zhou et al. (2015)]. Similar MPB region is also reported in $xPbTiO_3$-(1-x)$Bi(Ni_{1/2}Ti_{1/2})O_3$ [R. Pandey et al. (2014)]. XRD patterns of PT-BNN compositions with higher doping of BNN shows very small minor impurity phase (less than 1%) as marked by asterisk in Fig. 3.1 (a) which may be due to loss of volatile bismuth.

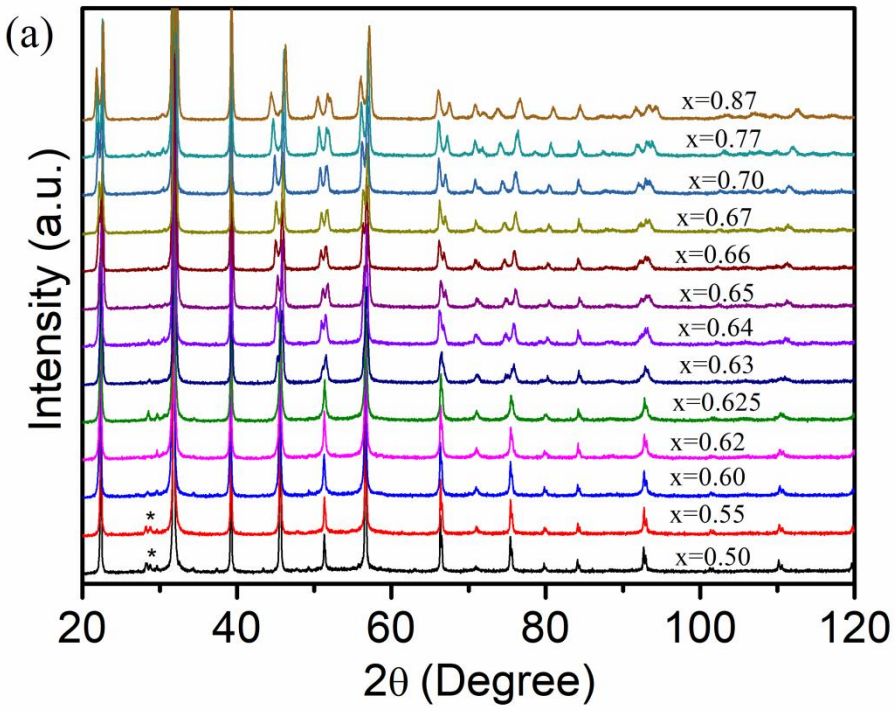

Figure 3.1 (a) Powder XRD patterns of various compositions of $xPbTiO_3$-(1-x)$Bi(Ni_{2/3}Nb_{1/3})O_3$ solid solution.

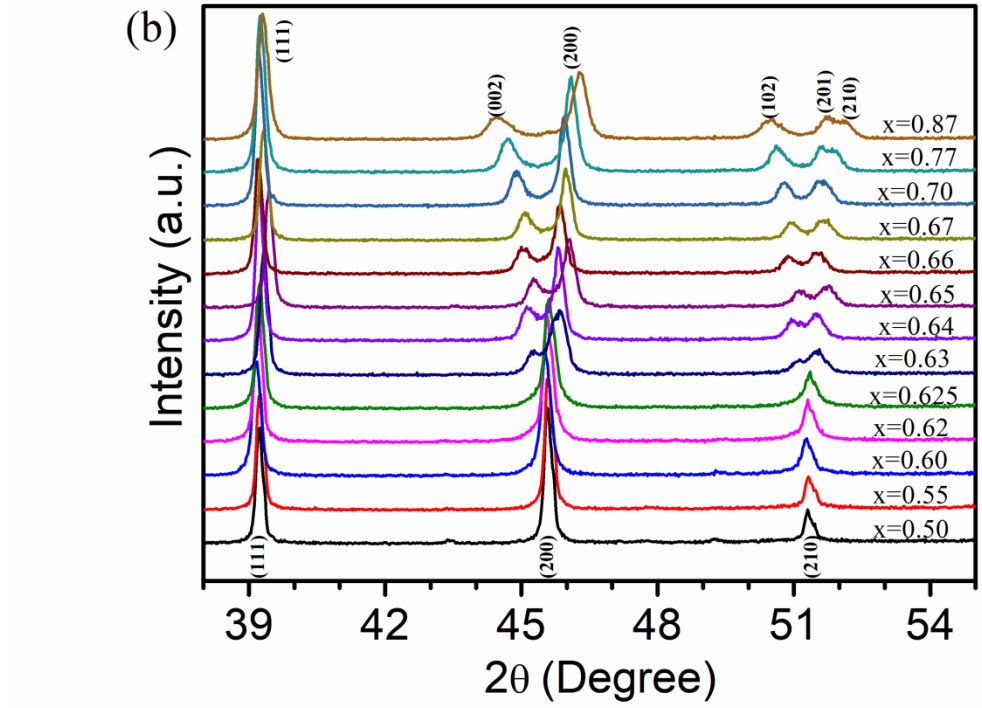

Figure 3.1 (b) Magnified Powder XRD profiles of (111), (200) and (210) reflections for $xPbTiO_3$-(1-x)$Bi(Ni_{2/3}Nb_{1/3})O_3$ solid solution.

Rietveld refinement of the X-ray diffraction patterns has been carried out using FullProf Suite to confirm the crystal structures. Rietveld refinement confirms that the samples 0.50PT-BNN to 0.62PT-BNN ceramics crystallize into single phase of rhombohedral structure with *R*3*m* space group, while samples 0.63PT-BNN to 0.87PT-BNN exhibit coexistence of tetragonal with *P*4*mm* space group and rhombohedral structure with space group *R*3*m*. These show that the morphotropic phase boundary (MPB) exhibits between the compositions x = 0.63-0.87. Obtained refined lattice parameters and unit cell volume for both structures and all samples are listed in Table 3.1. Tetragonality of the ceramic samples increases as the $PbTiO_3$ content is increased in PT-BNN.

Table 3.1: Refined lattice parameters (a, b, c) and unit cell volume (V) for PT-BNN ceramics.

Sample	Tetragonal (*P*4*mm*)			Rhombohedral (*R*3*m*)		
	a=b (Å)	c (Å)	V (Å^3)	a=b (Å)	c (Å)	V (Å^3)
0.50PT-BNN				5.6390(1)	6.9035(4)	190.11(1)
0.55PT-BNN				5.6362(2)	6.9013(3)	189.86(1)
0.60PT-BNN				5.6288(2)	6.8930(4)	189.14(1)
0.62PT-BNN				5.6279(2)	6.8978(7)	189.21(2)
0.625PT-BNN	3.9787(2)	3.9896(4)	63.155(8)	5.6296(2)	6.879(1)	188.82(3)
0.63PT-BNN	3.9708(2)	3.9998(3)	63.065(6)	5.6393(4)	6.972(2)	192.01(7)
0.64PT-BNN	3.9654(1)	4.0176(2)	63.173(3)	5.6314(1)	6.955(2)	191.02(5)
0.65PT-BNN	3.9638(2)	4.0267(2)	63.267(5)	5.654(1)	6.8976(4)	190.99(6)
0.66PT-BNN	3.9584(1)	4.0261(2)	63.084(5)	5.6433(4)	6.8933(4)	190.12(2)
0.70PT-BNN	3.9511(1)	4.0374(2)	63.028(3)	5.6453(3)	6.8852(6)	190.03(2)
0.77PT-BNN	3.9400(1)	4.0549(2)	62.947(3)	5.6436(4)	6.8836(8)	189.87(3)
0.87PT-BNN	3.9264(1)	4.0727(2)	62.789(5)	5.6448(5)	6.8769(6)	189.77(3)

The structural changes in PT-BNN ceramics were further analyzed by Raman spectroscopy which is sensitive to the local symmetry of crystalline structures. The Raman spectrum of PT-BNN resembles that of other ABO_3-type ferroelectric oxides. $PbTiO_3$ have Raman-active modes of tetragonal ferroelectric structures ($3A_1(TO) + 3A_1(LO) + 3E(TO) + 3E(LO) + 1E(LO + TO) + 1B_1$) [G. Burns et al. (1973)]. Fig. 3.2 shows the Raman spectra of PT-BNN solids solution for some representative compositions in the range x = 0.87-0.55. Two Peaks near 60 cm^{-1} and 785 cm^{-1} are related to cubic F_{2g} mode involving A-cation vibrations and A_{1g} symmetric stretching of BO_6 octahedra. The Raman scattering in the range 700-800 cm^{-1} is attributed to symmetrical BO_6 stretching which generates A_{1g} mode in the cubic $Pm\bar{3}m$ structure.

Raman scattering peaks near 270 cm^{-1} and 480 cm^{-1} are attributed to the off-centring of the B-site cations and indicate the existence of local ferroic distortions [I. G. Siny et al. (1998)]. It is observed that A_1(2TO) mode disappear for compositions x=0.60 due to broadening of the E_1+B_1 mode. Siny et al. (1998) have reported that the Raman active modes A_{1g}+E_g+$2F_{2g}$ disappear in the cubic perovskite phase. This indicates that an observed phase transition in the XRD result is consistent with the results of Raman studies. The peak position of soft mode E(1TO) shifts to lower frequency range with increasing the BNN concentration. Similar observation is also reported by da Costa et al for Ni doped $PbTiO_3$ ceramics as incorporation of Ni atoms in $PbTiO_3$ lattice create strain [R. C. da Costa et al. (2017)]. The E(1TO) mode is due to vibrations of Pb against the oxygen dodecahedral. The peaks related to E(1TO), E(1LO), E(2TO) and (B_1+E) shows broadening with increasing BNN doping which can be attributed to lattice distortion and increased disorder.

As illustrated in Fig 3.2 (b), presence of Raman peaks near 270 cm^{-1} and 480 cm^{-1}indicates the existence of local ferroic distortion. The Raman peaks mentioned as R1 in Fig. 3.2 (b) in spectral range 30 to 100 cm^{-1} is attributed to off-centred A-site cations vibrations. Peak R2 in spectral range 100-205 cm^{-1} is due to BO_6-translations against the A-site cation vibrations and it is termed as A-BO_6 mode [K. Datta et al. (2017); E. Buixadiras et al. (2015)]. The peaks R3 and R4 in spectral range 205-305 cm^{-1} are attributed to off-cantered B-site cations vibrations. Peak R5 near 330 cm^{-1} is due to tilting of BO_6 octahedra. Raman peaks R6, R7 and R8 in spectral range 410 to 800 cm^{-1} are attributed to internal BO_6 mode and is related to oxygen vacancies. Peak R6 is due to O-B-O bending and peak R8 at 720 cm^{-1} is related to stretching of BO_6 mode [I. Margaritescu et al. (2020)].

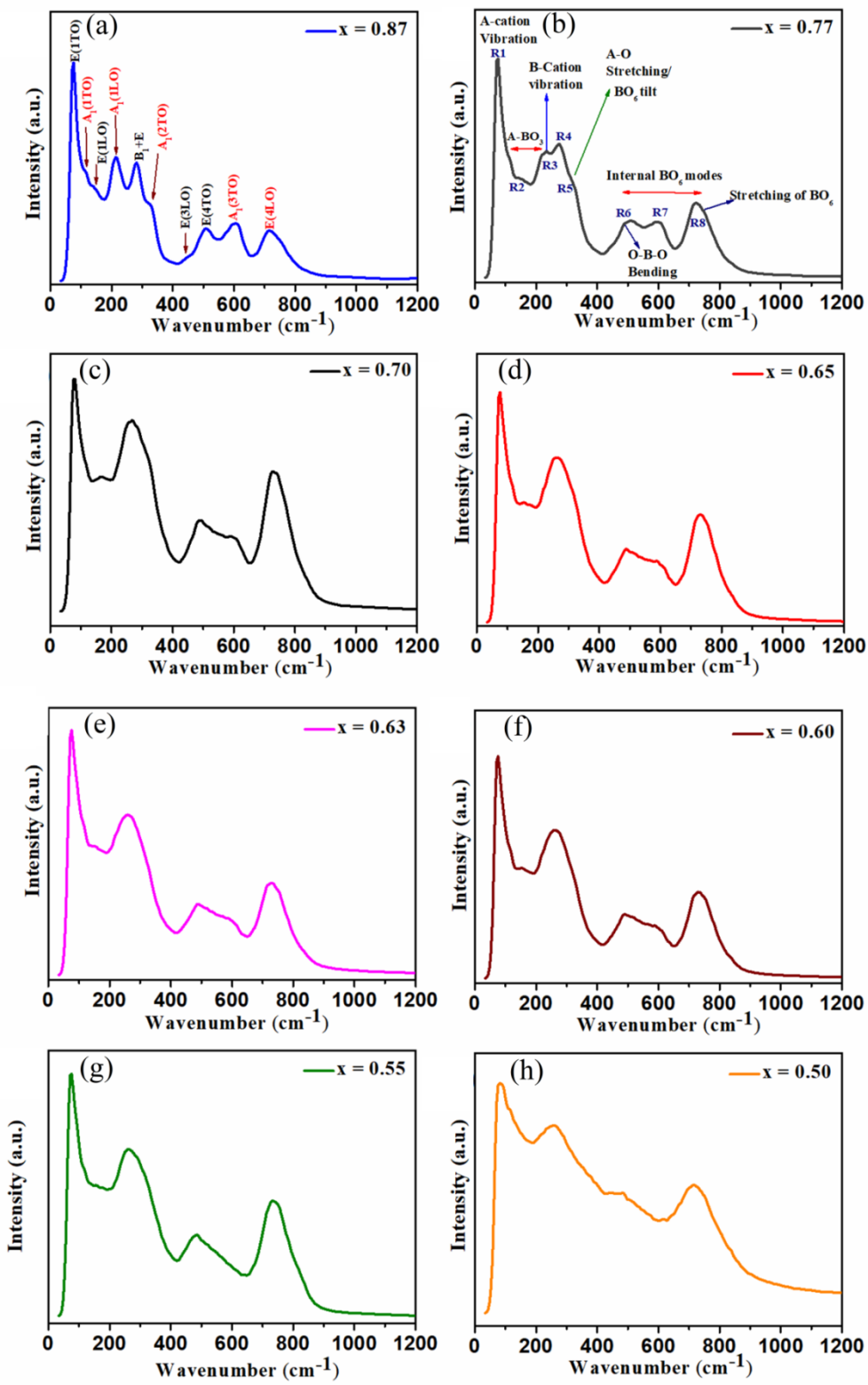

Figure 3.2 Room temperature Raman scattering spectra of $xPbTiO_3$-(1-x)$Bi(Ni_{2/3}Nb_{1/3})O_3$ solid solution for representative compositions (x = 0.87 to 0.50).

The composition dependent changes observed in Raman spectra are shown in Fig 3.2 (a) to 3.2 (h). The peak position tends to decrease with incorporation of Bi/Ni/Nb ions in PT lattice which shows reduction in ferroelectric properties. Raman mode E(1TO) first shifted to lower wavenumber with increasing the BNN doping and then show slight increase for compositions $x \leq 0.60$. Raman mode A1(2TO) is related to tetragonal phase and shifts to lower wave function and confirm the phase transformation with BNN doping. Similar behaviour is also reported for PT-BNT and it is proposed that there is coupling processes within the A-cation subsystem [I. Margaritescu et al. (2020)]. The broadening of A-BO_6 mode with BNN doping shows the coupling between the sublattices of off-centered A-site and B-site cations [K. Datta et al. (2017)]. As doping concentration increases, E(2TO) mode and quasi mode merges into (B1+E) mode which is related to the suppression of the prominent tetragonal distortion within the BO6 octahedra. Thus, we can conclude that changes observed in Raman spectra of PT-BNN are signature of phase transition from tetragonal to rhombohedral/pseudo-cubic phase in this solid solution similar to the observations of XRD studies.

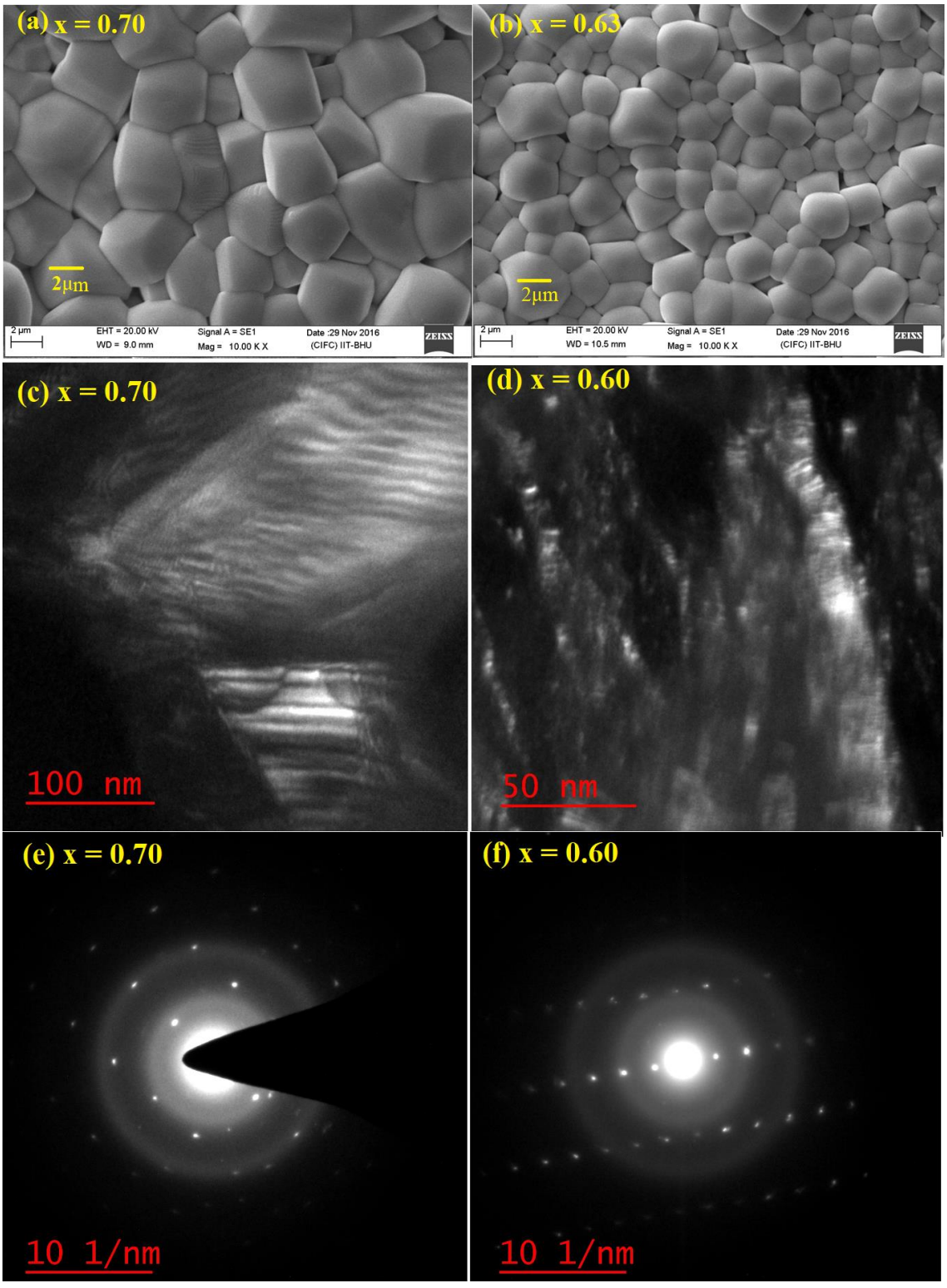

Figure 3.3 The Scanning electron microscopy (SEM) images ofPT-BNN for (a) x = 0.70 and (b) x = 0.63 compositions. Dark HRTEM image for (c) x = 0.70 and (d) x = 0.60 and (e) (f) the corresponding SAED pattern.

The morphology of PT-BNN solid solutions were studied using FE-SEM and HR-TEM measurement. The FE-SEM images of PT-BNN with varying BNN concentration are shown in Fig. 3.3 (a) and (b) for x=0.70 and 0.63 respectively. As can be seen in these figures, the microstructure is very dense, uniform and grain size is decreased with increasing BNN concentration. The grain size for composition x = 0.70 is about 4 to 5 μm and those for x = 0.63 is about approximately 2 to 3 μm. Increased densification at lower temperatures in presence of Bi is attributed to the reduced grain size with increasing the BNN concentration in PT. The decrease in grain size can also be related to the enhanced strain and defects in the PT lattice by BNN doping which inhibits the grain growth. Also, Nb^{5+} reduces the grain growth by slowing down the speed of oxygen ion as Nb^{5+} ions suppress the oxygen vacancies [T. Wang et al. (2016)]. The lower valence of doped Ni^{2+} ion than that of Ti^{4+} ion also leads to lower grain growth rate. As the grain size decreases with increasing the BNN doping, there is possibility of formation of insulating grain boundary between the grains. The insulating grain boundaries can slow down the current conduction and reduce the leakage current.

Fig. 3.3 (c) and (d) shows the dark field HRTEM image of PT-BNN ceramics for compositions x= 0.70 and x = 0.60. From the dark field image, the certain crystal orientations can be seen. The small lamellar like ferroelectric domains with domain wall (90°& 180°) are observed for x = 0.70 composition which conform to the tetragonal crystal symmetry. For composition x=0.60, the domains become narrow with predominately 71° domains indicating the rhombohedral structure. Fig 3.3 (e) and (f) shows the SAED patterns for composition x =0.70 and x = 0.60 where several sharp concentric rings and spots are observed.

3.3.2 Composition Dependent Dielectric and Ferroelectric properties of $xPbTiO_3$–$(1–x)Bi(Ni_{2/3}Nb_{1/3})O_3$ solid solution

Fig. 3.4 shows the plots of the temperature dependent relative permittivity (ε_r) for selected compositions of xPT-(1-x)BNN (x = 0.87, 0.77, 0.70, 0.65, 0.62, 0.60, 0.50) measured at different frequencies. The PT-BNN shows higher permittivity at lower frequencies as various polarizations such as interface, ionic, dipolar, electronic and space charge play combined role to increase the permittivity. But, at higher frequencies only electronic polarization contribute to ε_r value thus decline in ε_r is observed as frequency increases from 1kHz to 100kHz. Fig. 3.4 (a) shows the temperature dependent relative permittivity of xPT-(1-x)BNN for composition x = 0.87. At 100 kHz applied frequency, The permittivity increases with increasing temperature up to 456°C and then decline is started. The temperature at which maximum permittivity is obtained is called Curie temperature. Fig. 3.4 (b) shows the permittivity for composition x = 0.77. At 5 kHz applied frequency, the peak maximum temperature (T_m) is 428°C and it reduced to 418°C for 1000 kHz applied frequency suggesting relaxor nature of phase transition. Fig. 3.4 (c) shows the permittivity for composition x = 0.70 with similar relaxor characteristics. It is observed that the compositions with higher BNN concentration exhibit strong frequency dispersion which indicates that the relaxor ferroelectric behaviour is enhanced with increasing BNN. The highest room temperature ε_r of 4163 was obtained at 100 kHz for composition x = 0.65 as shown in Fig 3.4 (d). The increase in relative permittivity with increasing the measurement temperature below T_m (270°C for x = 0.65 composition) is due to increased dipolar polarizability with and thus increase in ε_r with increasing the measurement temperature. The compositions with x=0.60, and 0.50 show two permittivity maximum peak in temperature dependence. The first peak corresponds to dielectric relaxation and second

peak due to ferroelectric phase transition as reported in many other solid solutions [N. K. Verma et al. (2019)]. Fig 3.4 (g) and (h) show the dielectric loss as a function of temperature at different frequencies for x=0.87 and 0.50 compositions respectively. The dielectric loss is below 2 and decreases with increasing the frequency from 1kHz to 10^6 Hz. The dielectric loss shows higher values above Curie temperature.

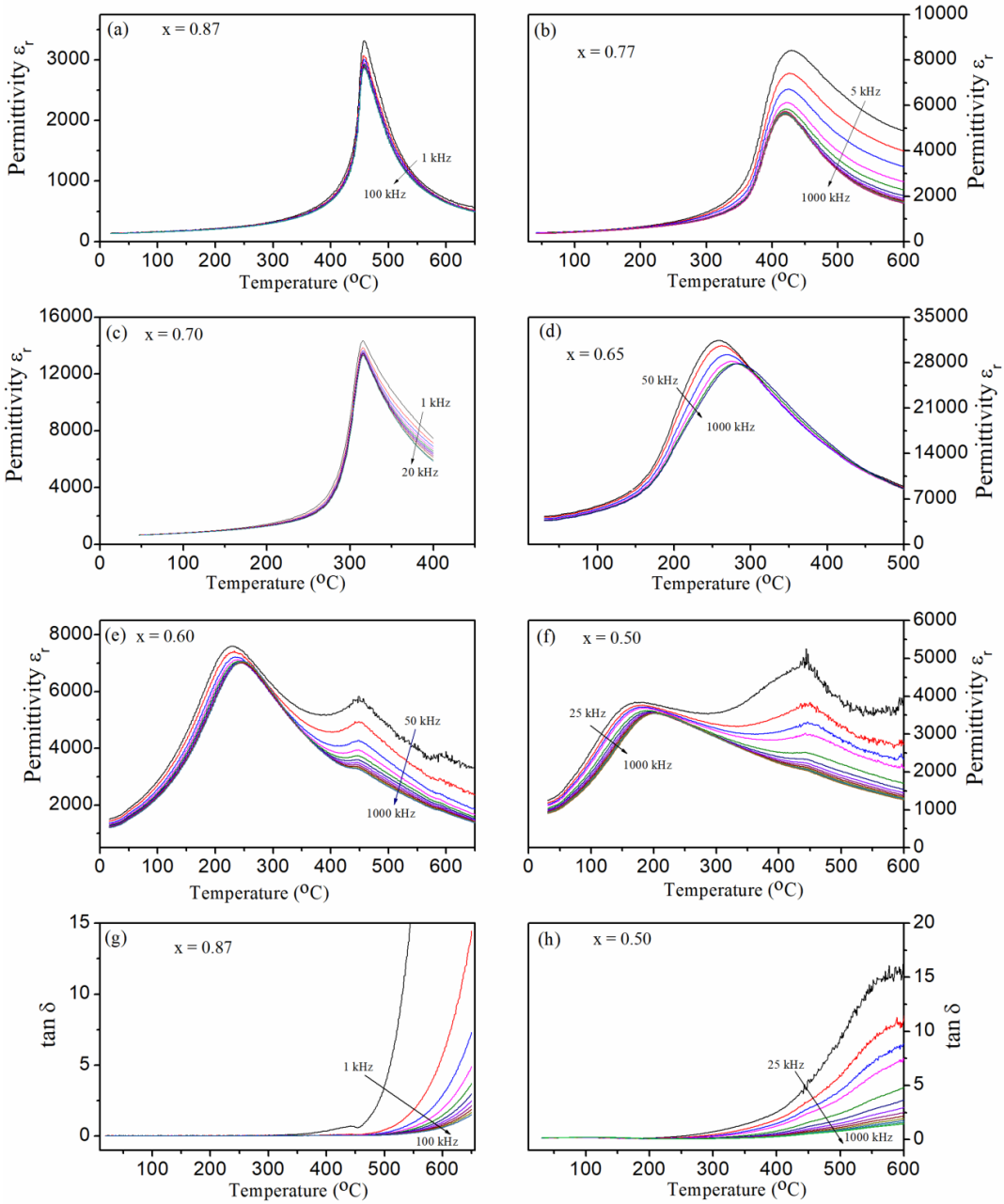

Figure 3.4 Temperature dependent permittivity of xPT-(1-x)BNN as a function of frequency for compositions (a) x = 0.87 to (f) x = 0.50 and temperature dependent dielectric loss for compositions (g) x = 0.87 and (h) x = 0.50.

Fig. 3.5 (a) display the compositional dependence of Curie temperature for xPT-(1-x)BNN measured at 100kHz frequency. It is observed that the composition with x = 0.87 has the highest Curie temperature, which is about 456°C and decreases to the lowest T_c (181°C) for the composition x = 0.50.The Curie temperature in MBP region is around 270°C. The T_c is directly related to tetragonality which decreases with increasing the BNN content. Thus, T_c decreases due to low tetragonality means small distorted lattice symmetry will require lower temperature to eliminate the crystalline distortion as compared to highly tetragonal compositions (x = 0.87) [D. M. Stein et al. (2006)]. The T_c for pure $PbTiO_3$ is reported to be 490 ^oC. Fig. 3.5 (b) shows the compositional dependence of room temperature dielectric permittivity which increases with increasing the BNN content reaches a maximum value corresponding to MPB and then reduces further. The maximization of dielectric permittivity confirms the MPB region around x = 0.60 to x = 0.70, for xPT-(1-x)BNN ceramics.

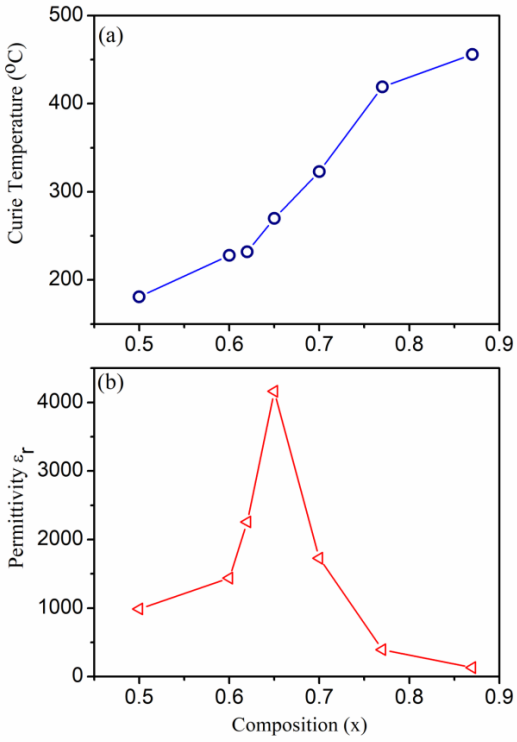

Figure 3.5 (a) Curie temperature and (b) Dielectric permittivity for xPT-(1-x)BNN as a function composition measured at 100kHz frequency.

Fig. 3.6 shows room temperature polarization (P)-electric field (E) hysteresis loops of some representative compositions of xPT-(1-x)BNN [x = (a) 0.87, (b) 0.77 (c) 0.70 (d) 0.65 (e) 0.625 (f) 0.50] measured up to E= 60 kV/cm at applied frequency of 1Hz. In 0.87PT-0.13BNNcomposition a remanent P_r value of 1.64 μC/cm^2 and E_c of 13.9 kV/cm are observed while the composition 0.77PT-0.23BNN have larger P_r (=12 .4 μC/cm^2) and E_c (=31.4 kV/cm) as shown in Fig. 3.6(a), (b). The low P_r value for 0.87PT-0.13BNN composition may due to large leakage currents of the capacitor which makes the 0.87PT-0.13BNN ceramic difficult to be fully polarized. The MBP region composition 0.65PT-0.35BNN shows the highest value of remnant polarization (P_r = 25.6 μC/cm^2) but the E_c (~ 28.2 kV/cm) is slightly reduces as compared to the composition with x = 0.70.The composition with x=0.625 also shows the high remanent polarization (P_r = 22 μC/cm^2), so it can be concluded that MPB region lies between x = 0.60 to x =0.70. The high polarization is related to presence of strong ralaxor features as observed in temperature dependent dielectric permittivity of these compositions. The observation of slim P-E loop for composition x = 0.50, is due to strong ralaxor features in high BNN composition. Fig. 3.7 shows the I-E switching current loops for x=0.65 and 0.625 that clearly excludes any possibility of charge injection.

Fig. 3.8 shows the ferroelectric hysteresis loops of 0.65PT-0.35BNN ceramics at various temperatures measured at 5Hz frequency. With increasing the measurement temperature from 50°C to 110°C, the P_r values are increased while E_c is decreased. At 50°C temperature, the P_r value is around 33 μC/cm^2 while it increases to 46 μC/cm^2 at measurement temperature of 110°C. Little lossy nature of P-E loops is also seen at the higher measurement temperatures which can be attributed to the enhanced defect induced conduction at higher temperatures.

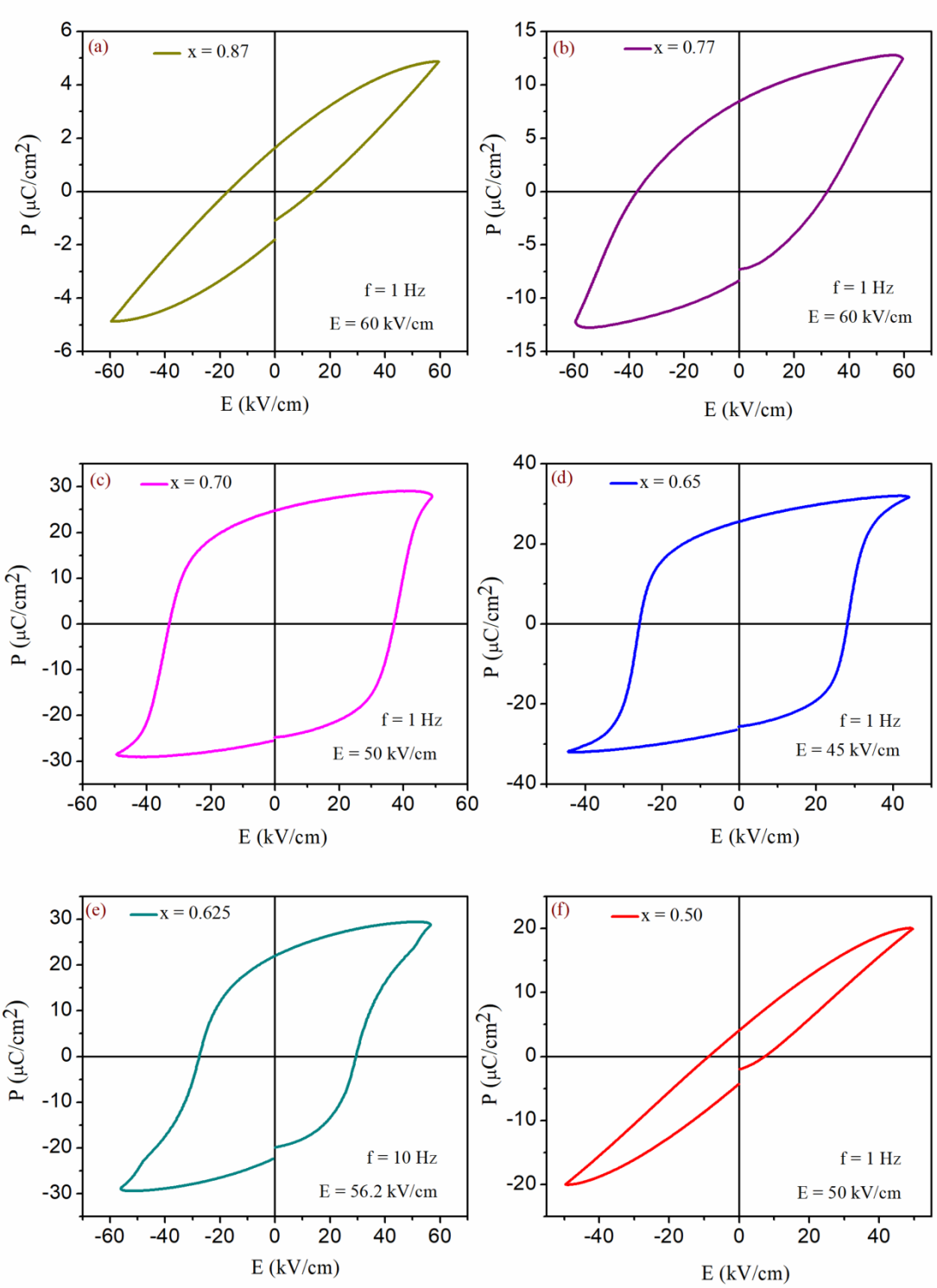

Figure 3.6 Room temperature P-E hysteresis loops of various compositions of xPT-(1-x)BNN ceramics (a) x = 0.87, (b) 0.77 (c) 0.70 (d) 0.65 (e) 0.625 (f) 0.50.

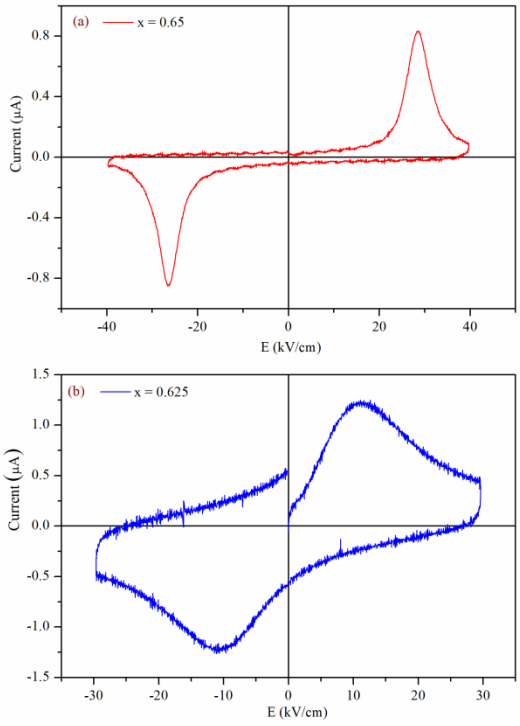

Figure 3.7 Room temperature I-E hysteresis loops of the xPT-(1-x)BNNfor (a) x = 0.65, and (b) x=0.625.

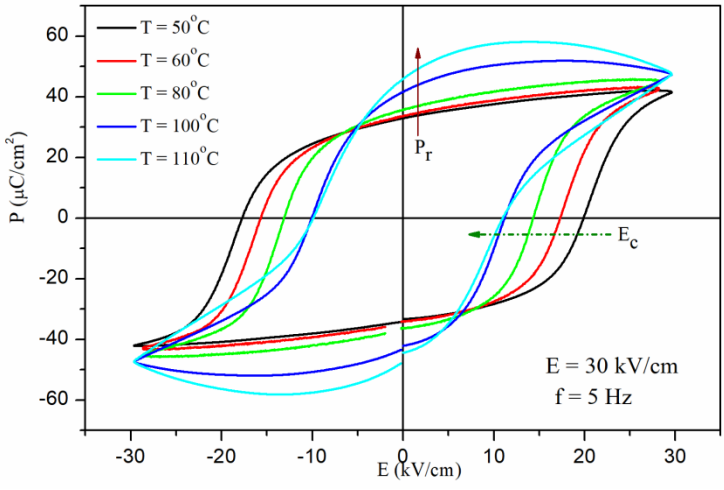

Figure 3.8 Temperature dependent P-E hysteresis loopsof 0.65PT-0.35BNN measured at 5 Hz frequency.

3.3.3 Composition Dependent Optical Band gap analysis

The influence of BNN doping percentage on the optical band gap of $xPbTiO_3$-$(1-x)Bi(Ni_{2/3}Nb_{1/3})O_3$solid solution for different compositions (x = 0.87, 0.77, 0.70, 0.65, 0.63, 0.60, 0.55) is supported by optical absorption spectra as shown in Fig. 3.9. We observe that the BNN doped $PbTiO_3$ compositions show multi-absorbance peaks mentioned as A1, A2, A3 and A4 in Fig. 3.9 (a). The A1 and A4 peaks are not fully covered in the measured wavelength range. The PT-BNN solid solution has very broad absorption peak (A2) in visible range. The absorption peak A2 (667-738 nm) and A3 (798-840nm) are attributed to Ni doping and are main cause for semiconducting nature of PT-BNN. Peak A4 lies in the NIR range and is due to oxygen vacancies created by the existence of Ni^{2+} [C. Li et al. (2018)]. The undoped $PbTiO_3$ have absorbance peak at 400 nm which shifts toward a larger wavelength (417-498 nm) with increasing the BNN doping percentage. This shift of absorption edge toward larger wavelength is indication of lowering the optical band gap. The Tauc equation $(\alpha h\upsilon)^2$ vs $h\upsilon$for direct band gap provides band gap values. The band gap of all compositions was determined by extrapolating the linear part of the $(\alpha h\upsilon)^2$ versus $(h\upsilon)$ plots, where $h\upsilon$ is band gap energy and α is absorption coefficient [J. Tauc et al. (1966)] as shown in Fig. 3.9(b). The undoped $PbTiO_3$ shows an optical band gap of 2.9 eV which reduces to 2.46 eV for composition x = 0.87. Two different band gap E_{g1} = 2.46 eV and E_{g2} = 1.27 eV were featured in $(\alpha h\upsilon)^2$ vs $h\upsilon$plot for x=0.87composition. Both band gap values reduce to E_{g1} = 2.27 eV and E_{g2} = 1.25 eV for x=0.70 composition. The MPB composition (x = 0.65) shows slightly increased value of band gap (E_{g1}= 2.3 eV). The band gap values increased with further doping of BNN as can be seen in inset of Fig. 3.9 (b). The direct band gap E_{g1} arises from p-d charge-transfer excitations.

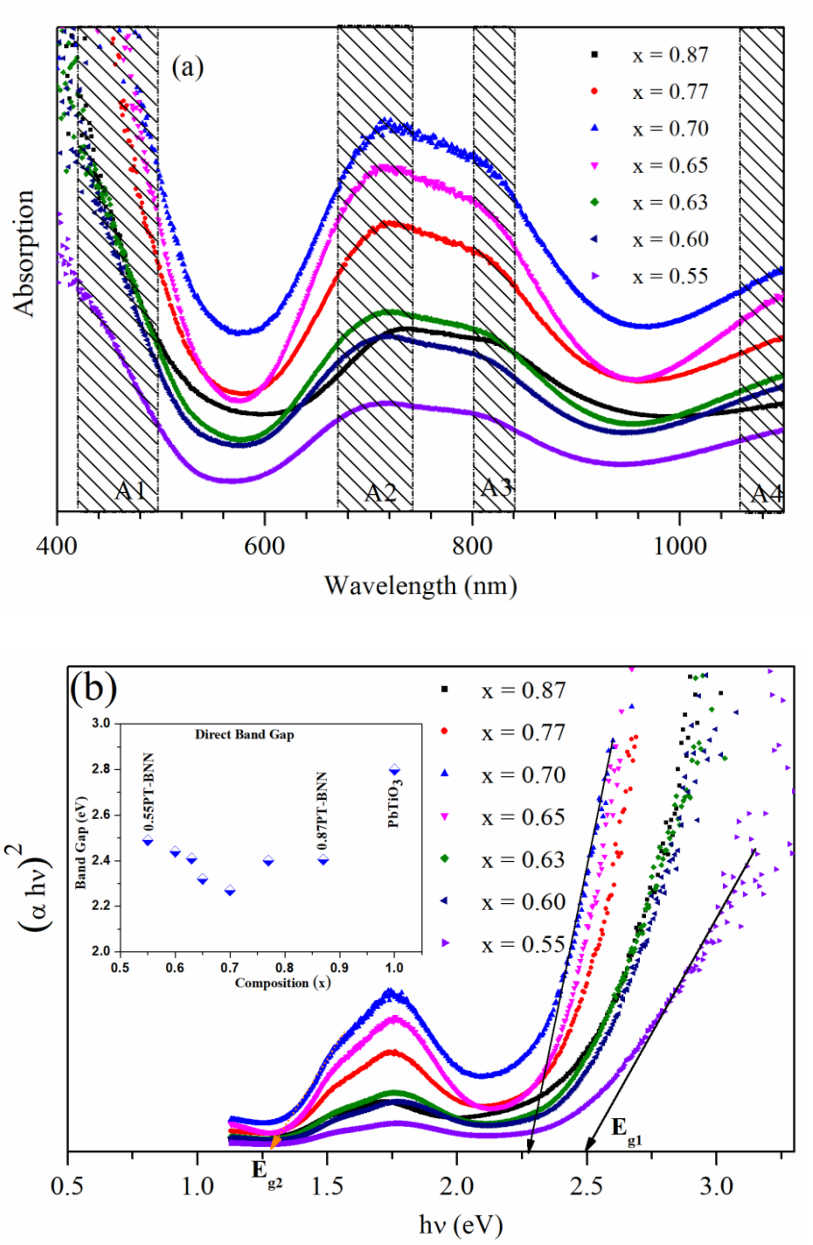

Figure 3.9 Composition dependent variations of (a) absorption spectra (b) direct band gap estimation using the Tauc plot $(\alpha h\upsilon)^2$ vs hυ for $xPbTiO_3$-(1-x)$Bi(Ni_{2/3}Nb_{1/3})O_3$solid solution for compositions in the range ($0.55 \leq x \leq 0.87$).

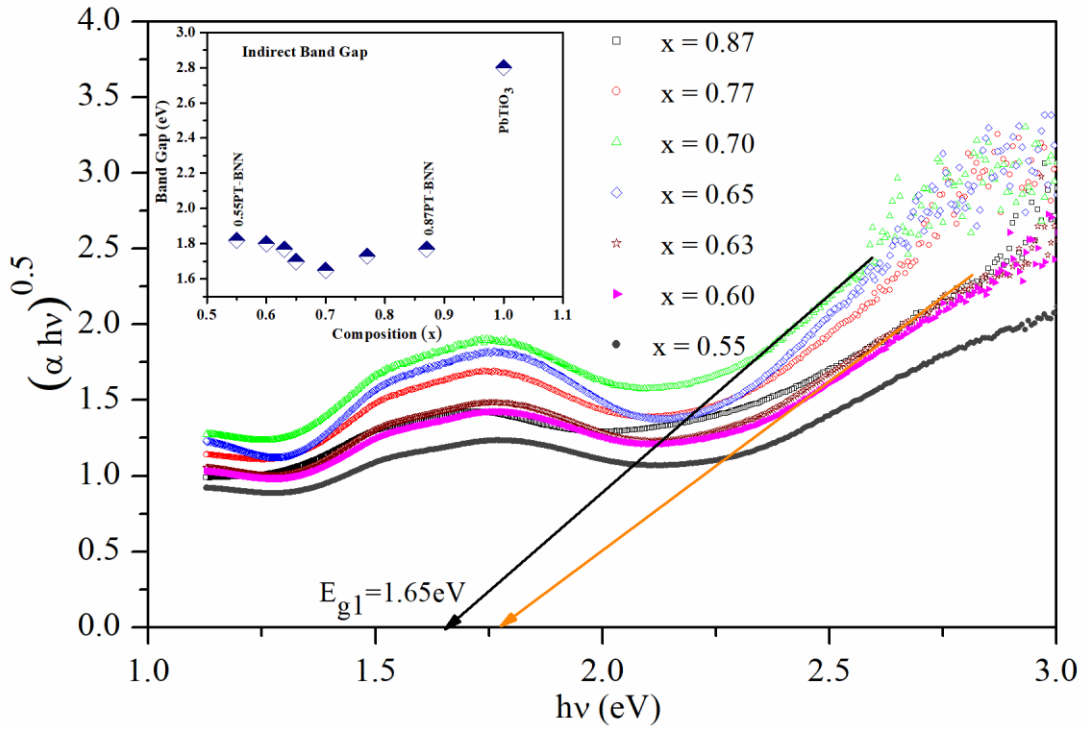

Figure 3.10 Composition dependent variations of Indirect band gap estimation using the Tauc plot $(\alpha h\upsilon)^{0.5}$ vs hυ for $xPbTiO_3$-(1-x)$Bi(Ni_{2/3}Nb_{1/3})O_3$solid solution.

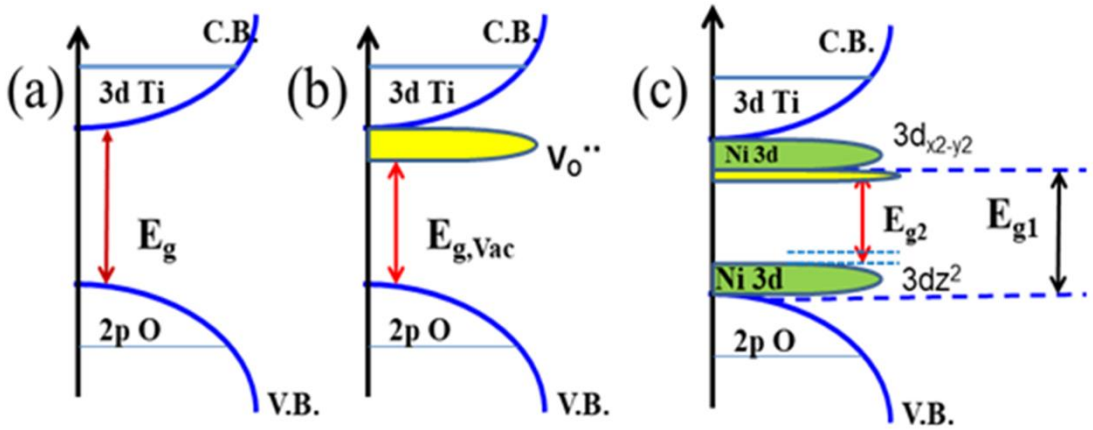

Figure 3.11 Schematic diagram of density of electronic states (a) Ideal Situation for $PbTiO_3$ (b) With presence of oxygen vacancies (c) with presence of Ni states and oxygen vacancies $xPbTiO_3$-(1-x)$Bi(Ni_{2/3}Nb_{1/3})O_3$.

The band gap at lower energy side E_{g2} arises from hybridization of Ni ($3d_z^2$+O2p_z) and Ni 3d excitations [B. S. Holinsworth et al. (2015)]. The E_{g2} feature is weaker in intensity which may be due to low density of states. The decrease in band gap values with increasing the BNN content can be assigned to new states of valence band maximum ($3d_z^2$) and conduction band minimum ($3d_{x^2-y^2}$) in an electronic structure with presence of Ni-3d and oxygen vacancies [E. Mete et al. (2019)]. The Fig. 3.11 explains the mechanism of band gap lowering due to formation of sub-band between valence and conduction bands. The position of E_{g1} and E_{g2} band gap is explained by showing the sub-band states. The Tauc equation $(\alpha h\upsilon)^{0.5}$ vs $h\upsilon$ has been used to calculate the indirect band gap for $xPbTiO_3$-(1-x)$Bi(Ni_{2/3}Nb_{1/3})O_3$solid solution. The indirect band gap reduces to 1.65 eV for composition x = 0.70 and then start increasing after further increasing the BNN contents in $PbTiO_3$. As shown in Fig. 3.10, it is observed that after extrapolating the tangent it provides unrealistic values for E_{g2}.

3.3.4 Band Gap Narrowing in Ni doped $0.65PbTiO_3$-$0.35Bi(Ni_{2/3}Nb_{1/3})O_3$ Ferroelectric Ceramics

For ideal ferroelectric photovoltaic material, a low band gap and high polarization is necessary condition to increase the light absorption and also provide the large built-in-electric field for separating the photo-carriers. In section 3.3.2, it is obtained that x=0.65 composition shows very high polarization (P_r = 25.6 μC/cm^2) and direct band gap ~ 2.3 eV. To further reduce the band gap of x = 0.65 composition, we have modified the stoichiometric ratio of Ni and Nb by increasing the Ni concentration according the composition $0.65PbTiO_3$-$0.35Bi(Ni_{2/3+y}Nb_{1/3-y})O_3$ solid solutions with varying the Ni concentration (y = 0.04, 0.07, and 0.10). The band gap decreases with increasing the Ni concentration which is due to new states formed between valence band maximum (VBM) and conduction band minimum (CBM). The absorption spectra

of as prepared samples were measured at room temperature and direct band gap has been calculated from the Tauc plot as shown in Fig. 3.12 (a-d). The estimated values of direct band gap for Ni concentration y = 0.04, 0.07 and 0.1 are 2.26eV, 2.23eV and 2.37 eV. The optical band gap first reduces to 2.23 eV for y = 0.07 composition but later increased to 2.37 eV for y = 0.1 in $0.65PbTiO_3$-$0.35Bi(Ni_{2/3+y}Nb_{1/3-y})O_3$ solid solution. The reduced band gap can be related to substitution of the larger Ni^{2+} for smaller Nb^{4+} cations which expand the Ti/Ni/Nb-O_6 octahedra [H. Liu et al. (2015)]. The polarization-electric field (P-E) hysteresis loops for Ni doped 0.65PT-0.35BNN solid solutions is shown in Fig. 3.12 (e) and (f). With increasing the Ni concentration and reduction in Nb content the polarization of 0.65PT-0.35BNNdecreases. The high value of extra Ni content causes leakage currents in PT-BNN due to excess oxygen vacancies. Due to leakage current phenomenon the experimentally observed P_r values for y = 0.04 and y = 0.07 show reduction as compared to 0.65PT-0.35BNN. The reduced P_r in Ni doped 0.65PT-0.35BNN is attributed to domain wall mobility and leakage problem.

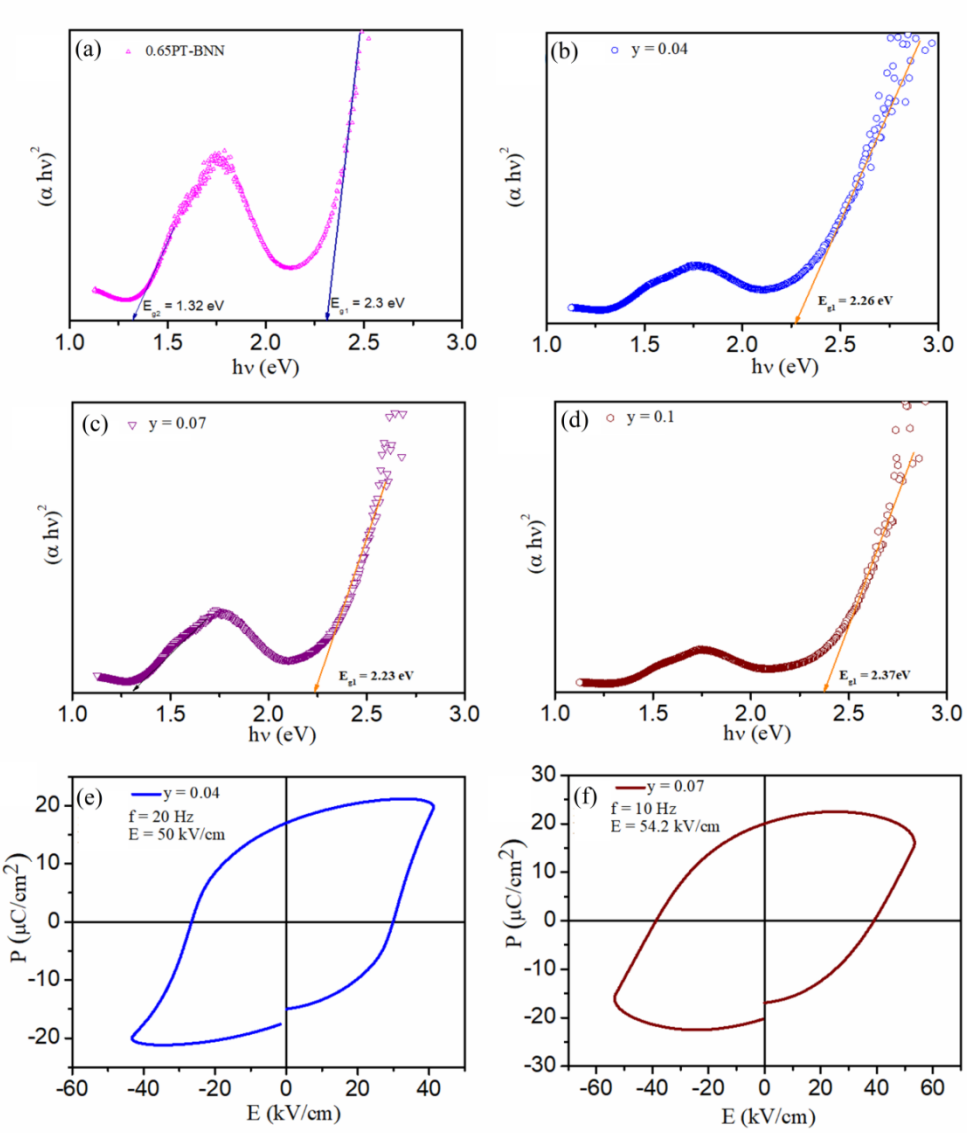

Figure 3.12 The Tauc plot $(\alpha h\upsilon)^2$ vs hυ for 0.65PT-0.35BNN solid solution (a) without Ni doping, and with Ni doping (b) y = 0.04, (c) y = 0.07 and (d) y = 0.1. P-E hysteresis loops of 0.65PT-0.35BNN doped with Ni (e) y =0.04 (f) y =0.07.

3.3.5 Band Gap Narrowing in Co doped $0.65PbTiO_3$-$0.35Bi(Ni_{2/3}Nb_{1/3})O_3$ Ferroelectric Ceramics

Another transition element Co has been also used to dope 0.65PT-0.35BNN by reducing the Ni percentage in ceramic because Co 3d-state is lower in energy than the Ti-3d states which can increase the tailing of conduction band edge and thus could reduce the band gap. The Co-doped 0.65PT-0.35BNN solid solutions are prepared according to the formula $0.65PbTiO_3$-$0.35Bi(Ni_{(2-y)/3}Co_{y/3}Nb_{1/3})O_3$ where y is varied as y = 0.0, 0.3, 0.6, and 1.0. The XRD profiles of these compositions are shown in Fig. 3.13. It is noticed that the tetragonality was increased with increasing the Co contents in 0.65PT-0.35BNN solid solutions. Even after Co doping, all the samples retain the perovskite structure. The Co-doped compositions show splitting of (200) reflection peak and also, gap between (002) and (200) peak increases with increasing the Co concentration as depicted in inset of Fig 3.13. The Tauc plot and polarization hysteresis loops of Co-doped 0.65PT-0.35BNN samples are presented in Fig 3.14. All compositions have well saturated hysteresis loops but remanent polarization decreases with increasing the Co content in samples. Thus, it can be possible that Co is degrading the ferroelectric behaviour of 0.65PT-0.35BNN perovskite. The decrease in remanent polarization can be attributed to leakage current in material due to extra oxygen vacancies created by introduction of Co ion. As can be observed from the Fig. 3.14 the band gap decreases from 2.3 eV to 1.55 eV with increase in Co concentration in 0.65PT-0.35BNN ceramic. The band gap further decreased to 1.5 eV for sample 0.65PT-0.35BNN (y= 0.1). The decrease in band gap could be related to increase in tetragonality as found in its XRD. It is apparent that the band gap of 0.65PT-0.35BNN perovskite can be reduced very effectively by the Co^{2+} doping. Ti_{Co} creates a new localized band below the conduction band minimum [Z. Pan et al. (2017), B. S. Holinsworth et al. (2015)].

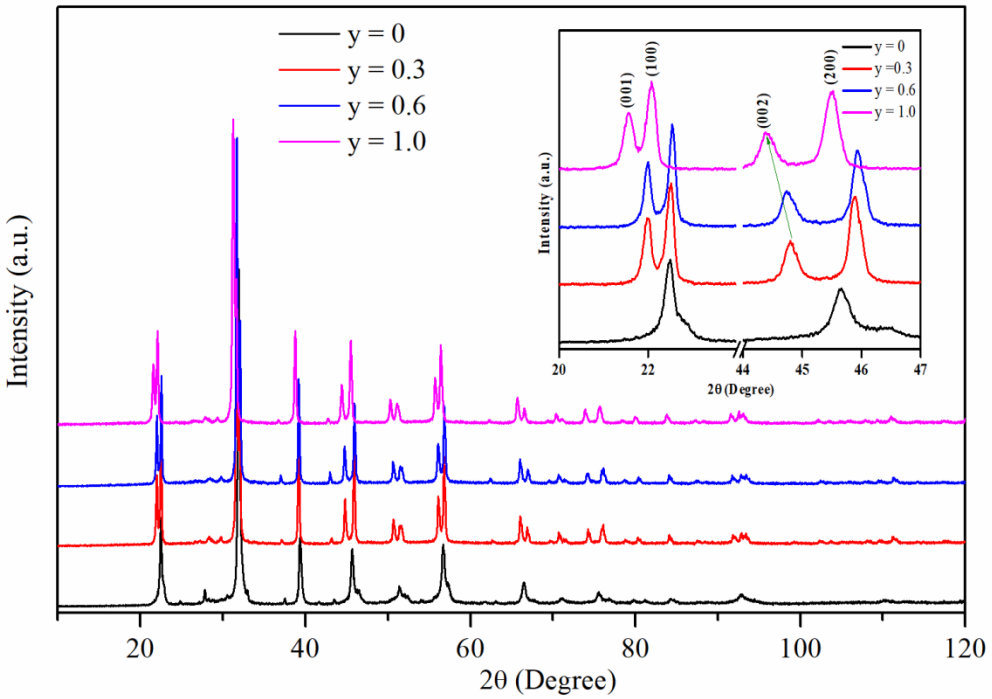

Figure 3.13 Powder X-ray diffraction patterns of $0.65PbTiO_3$-$0.35Bi(Ni_{(2-y)/3}Co_{y/3}Nb_{1/3})O_3$ with y = 0.0, 0.3, 0.6, and 1.0. Inset is showing the change in position of selected diffraction peaks with Co doping.

Till now, we have observed that the both Ni and Co are able to reduce the band gap of $PbTiO_3$. Ni and Co are transition elements with 3d orbital states which are identical to that of Ti. The ionic size of Co^{2+} and Ni^{2+} is smaller than that of Bi^{3+} but very close to that of Ti^{4+}, so, Co and Ni ions prefer to substitute the Ti sites in perovskite structure rather than occupying the Bi-sites. Thus, very significant band gap narrowing is obtained in Ni and Co doped 0.65PT-0.35BNN perovskites. The reduced band gap of Co doped 0.65PT-0.35BNN have motivated us to replace Ni in 0.65PT-0.35BNN with Co and design a new solid solution $xPbTiO_3$-$(1-x)Bi(Co_{2/3}Nb_{1/3})O_3$ (PT-BCN) with perovskite structure. The $Bi(Co_{2/3}Nb_{1/3})$ (BCN) cation is selected as transition metal ions in $PbTiO_3$-$BiMeO_3$ compounds. The Pb^{2+} and Bi^{3+} cations have $6s^2$ lone pair electron and they maintain the high remnant polarization in $xPbTiO_3$-$(1-x)Bi(Co_{2/3}Nb_{1/3})$ compositions while Co^{2+} ion act to reduce the band gap by

hybridization of Co-3d and O-2p. Similar band gap lowering is also reported in $BiCoO_3$ [M. Q. Cai et al. (2007)]. Fig. 3.15 (a) shows the Tauc plot [$(\alpha h\upsilon)^2$ vs $h\upsilon$] of as prepared PT-BCN ceramics. It is apparent that the band gap reduces with increasing the BCN contents in $PbTiO_3$. The band gap for 0.90PT-0.10BCN composition is estimated 1.5 eV which is much lower than parent $PbTiO_3$ ceramics. Further doping of BCN in $PbTiO_3$ again reduces the band gap and the lowest band gap (E_g = 1.3 eV) was obtained for 0.58PT-042BCN composition as shown in Fig. 3.15 (b). The reduced band gap can be explained by the mechanism of Co^{2+} doping induced band states in these perovskite oxides. The Co-ion with oxygen vacancies creates new states in the electronic structure between conduction band and valence band. In $PbTiO_3$, the conduction band is formed by presence of Ti-3d states and valence band (VB) is created by O-2p orbital states according to previous studies. When Co^{2+} is doped, both CB and VB get localized around Co-3d states and O-2p orbitals. Due to increased BCN doping, the extra Co-d_z^2 state and Co-d^2_{x-y} states are created between CB and VB which reduces the band gap of PT-BCN. The reduced band gap in PT-BCN ceramic is attributed to the interband transition from the d_z^2 state to the $d_{x^2-y^2}$ state [F. Azough et al. (2010)] and the electron transition in CoO_6 octahedra [H. Liu et al. (2017)].

The semiconducting nature of PT-BCN is analyzed by its temperature dependent electrical conductivity using impedance spectra. The ceramics have two types of resistance, bulk resistance and grain boundary resistance and the impedance spectra consists both elements (R_g and R_{gb}) in complex form.

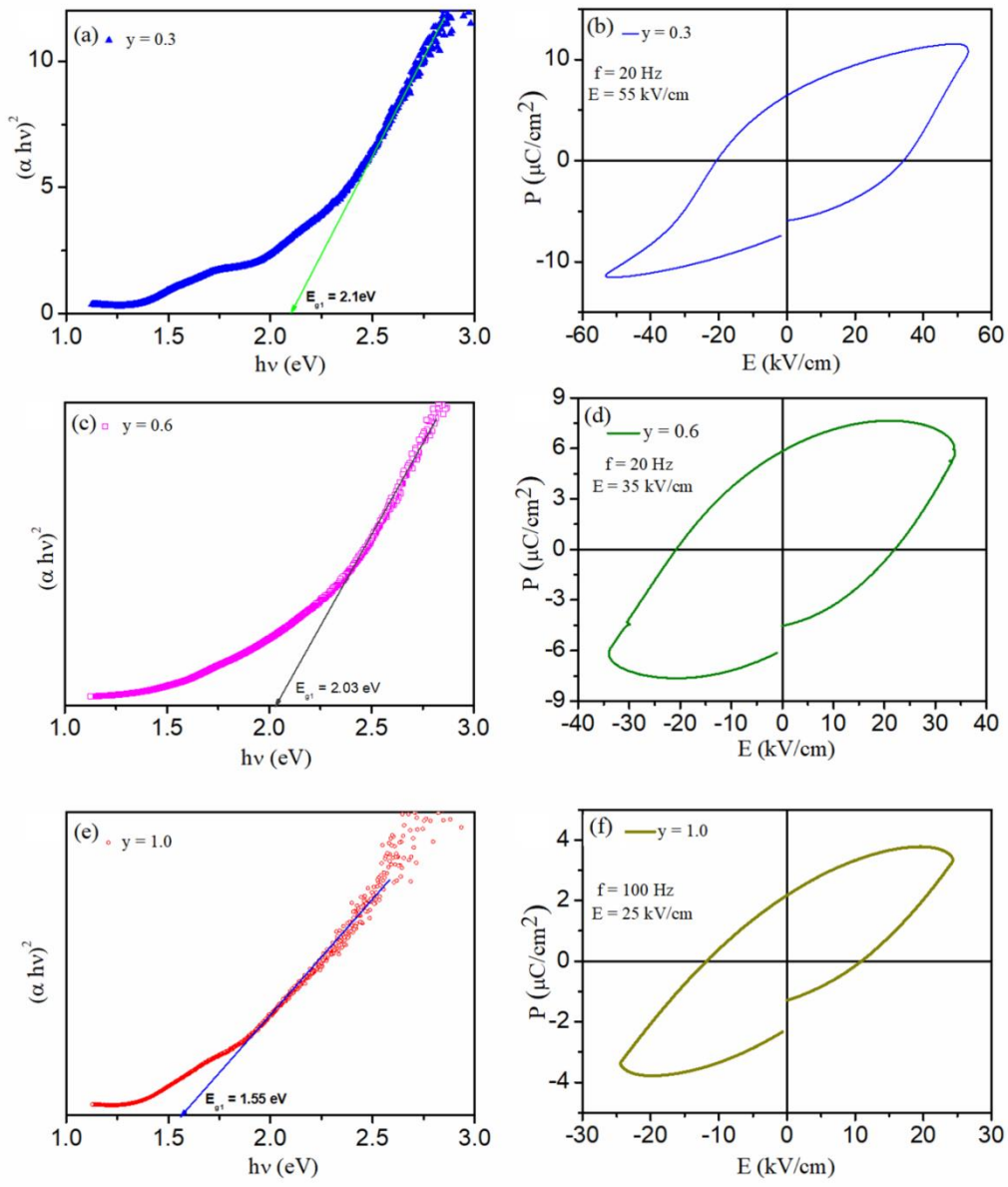

Figure 3.14 The Tauc plot $(\alpha h\upsilon)^2$ vs hυ and P-E hysteresis loops for $0.65PbTiO_3$-$0.35Bi(Ni_{(2-y)/3}Co_{y/3}Nb_{1/3})O_3$ with y = 0.3 (a), (b), 0.6 (c), (d) , and 1.0 (e), (f).

Fig. 3.15 (c) & (d) shows the Nyquist plot ($Z^{/}$ vs $Z^{//}$) of 0.90PT-0.10BCN and 0.60PT-0.40BCN measured at 100°C, 150°C, 160°C and 180°C. The obtained Nyquist plots consists two semi-circular arcs which consist the contribution of both R_g and R_{gb} elements of electrical resistivity. It is observed that both R_g and R_{gb} values decrease with increasing the measurement temperature which is due to thermally activated charge carriers in semiconducting materials. These results indicate that PT-BCN

ceramic can be considered as a ferroelectric semiconductor [Q. Xu et al. (2016)]. The inset of the Fig. 3.15 (c) shows the comparison between R_g and R_{gb} of 0.90PT-0.10BCN and 0.60PT-0.40BCN at fixed (150 ^oC) temperature. It is found that highly BCN doped 0.60PT-0.40BCN have lower resistance as compared to 0.90PT-0.10BCN. These results are in agreement with the lower band gap of 0.60PT-0.40BCN and show that BCN doping significantly decreases the band gap of $PbTiO_3$ and is a promising new semiconducting ferroelectric system for photovoltaic applications.

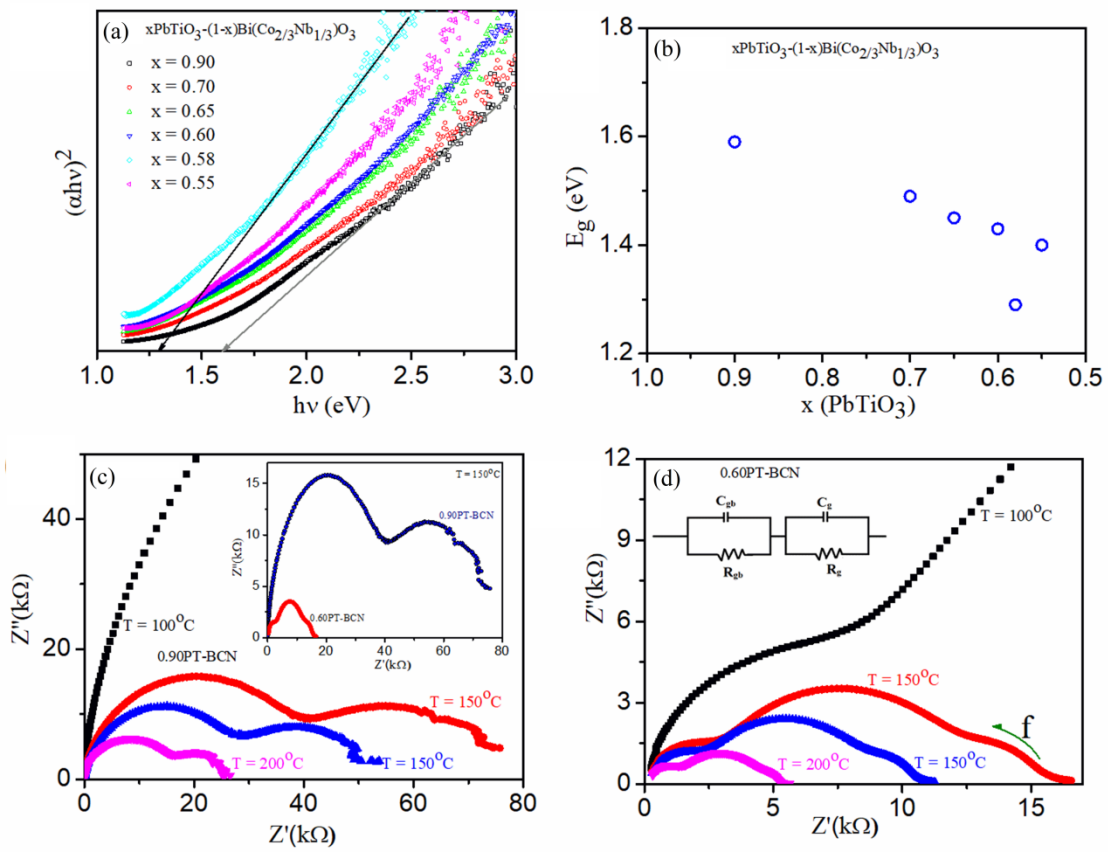

Figure 3.15(a) The Tauc plot $(\alpha h\upsilon)^2$ vs hυ and (b) Optical band gap for $0.65PbTiO_3$-$0.35Bi(Co_{2/3}Nb_{1/3})O_3$solid solution. (c) Nyquist plots of impedance spectra for $0.90PbTiO_3$-$0.10Bi(Co_{2/3}Nb_{1/3})O_3$ and (d) $0.60PbTiO_3$-$0.40Bi(Co_{2/3}Nb_{1/3})O_3$. The inset shows the equivalent circuit model grain boundary resistance (R_{gb}) and bulk resistance (R_g)

3.3.6 Band Gap Narrowing in Composites of $Ni_{0.65}Zn_{0.35}Fe_2O_4$ and $Co_{0.5}Zn_{0.5}Fe_2O_4$ With $0.65PbTiO_3$-$0.35Bi(Ni_{2/3}Nb_{1/3})O_3$ ceramics

To introduce the multiferroic character in the prepared ferro-photovoltaic material $0.65PbTiO_3$-$0.35Bi(Ni_{2/3}Nb_{1/3})O_3$, we prepared its particulate composites with $Ni_{0.65}Zn_{0.35}Fe_2O_4$ spinel magnetic ceramics. In this section of chapter, we have investigated the optical band gap and ferroelectric polarization of various compositions of multiferroic particulate composites of $0.65PbTiO_3$-$0.35Bi(Ni_{2/3}Nb_{1/3})O_3$ (0.65PT-0.35BNN) with $Ni_{0.65}Zn_{0.35}Fe_2O_4$ (NZFO) as (1-y) [0.65PT-0.35BNN]-yNZFO (y= 0.05, 0.10, 0.50 and 0.75). The XRD patterns of various compositions of (1-y) [0.65PT-0.35BNN]-yNZFO composites along with pure component phases are shown in Fig. 3.16. As described in section 3.3.1, the XRD patterns of 0.65PT-0.35BNN solid solution exhibit well defined sharp peak with tetragonal perovskite structure. The spinel NZFO exhibit cubic phase and it's XRD peaks are indexed in Fig.3.16. As can be seen from Fig.3.16, for all the compositions, there is only ferrite and ferroelectric phases of (1-y) 0.65PT-0.35BNN-yNZFO composites and no other impure phase is observed. No impurity peaks are observed for all the composite compositions, so no impure phase is formed during mixing the two different components. It is clearly seen in Fig. 3.16 that the introduction of spinel NZFO in ferroelectric 0.65PT-0.35BNN increases its tetragonality for the compositions with y = 0.05 and 0.10. As expected, with increasing the NZFO content in 0.65PT-0.35BNN, the intensity of XRD profiles corresponding to NZFO phase is increased while intensity of tetragonal phase of 0.65PT-0.35BNN is decreased.

The Tauc plots $(\alpha h\upsilon)^2$ vs $h\upsilon$ for various compositions of 0.65PT-BNN-yNZFO composites are shown in Fig.3.17 (a),(c), (e) and (g). As can be observed from the Fig. 3.17 (a) the band gap decreases from 2.3 eV to 1.85 eV with introduction of NZFO (y=0.05) in 0.65PT-0.35BNN ceramic.

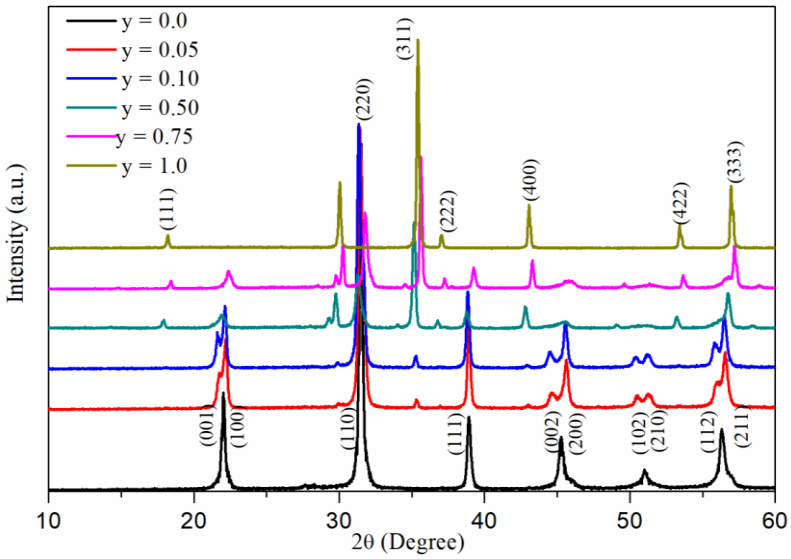

Figure 3.16 Powder XRD patterns of (1-y)[0.65$PbTiO_3$-0.35$Bi(Ni_{2/3}Nb_{1/3})O_3$]-y$Ni_{0.65}Zn_{0.35}Fe_2O_4$ particulate composites with y = 0, 0.05, 0.10, 0.50 , 0.75 and 1.0.

The band gap further decreases to 1.56 eV for the sample with y= 0.1. The decrease in band gap for these two compositions could be related to the increased tetragonality of ferroelectric phase, due to introduction of NZFO, as revealed clearly from the XRD pattern of these compositions shown in Fig.3.16. It is apparent that the band gap of 0.65PT-0.35BNN perovskite may be reduced due to electron excitation from O-2p into the Fe-3d level. For the compositions with y=0.50 and 0.75, the band gap again increases to higher values as 2.36 eV and 2.5 eV. This can be attributed to the decreased tetragonality of 0.65PT-0.35BNN for further higher concentration of NZFO in the composites. Fig. 3.17 (b, d. f, h) depicts the polarization–electric field (P-E) hysteresis loops for different compositions of (1-y) [0.65PT-0.35BNN]-yNZFO with y = 0.05, 0.10, 0.50, and 0.75. All the compositions show the ferroelectric hysteresis loops but remanent polarization and coercive field both are decreased with increasing the NZFO fraction in 0.65PT-0.35BNN solid solution, possibly due to dilution effect of ferroelectric phase.

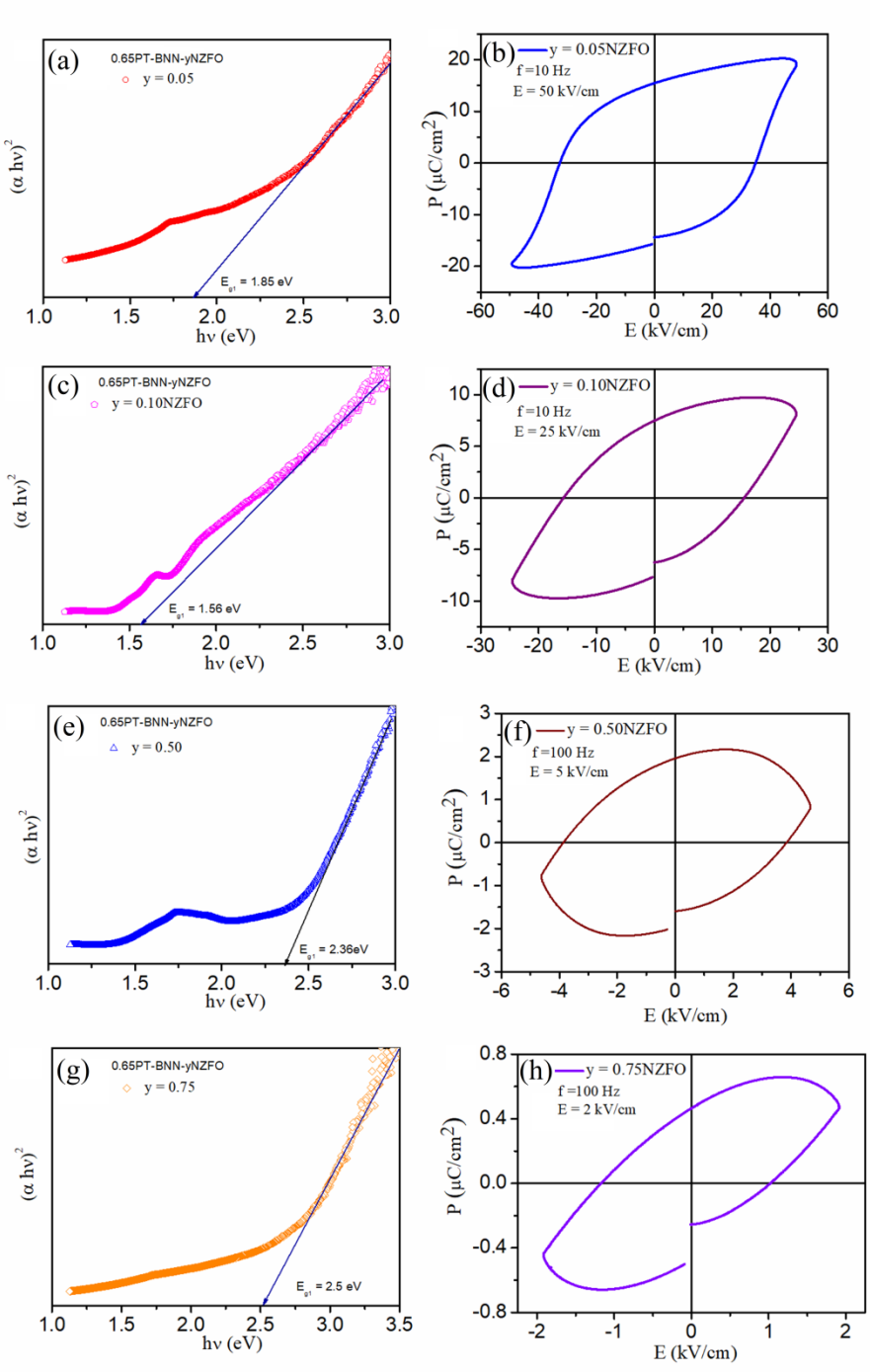

Figure 3.17 Tauc plot $(\alpha h\upsilon)^2$ vs hυ for 0.65PT-BNN-yNZFOcomposites with y = (a) 0.05 (c) 0.10 (e) 0.50 and (g) 0.75 and corresponding P-E hysteresis loop in (b), (d), (f) and (h).

After inspiring from Co doping in PT-BNN, we have also used Cobalt based spinel $Co_{0.5}Zn_{0.5}Fe_2O_4$ (CZFO) as magnetic component in **(**1-y)[0.65PT-0.35BNN]-yCZFO particulate composite with varying the (y =0, 0.05, 0.10, 0.50, 0.75 and 1.0), and investigated the band gap, as shown in Fig.3.18. The cubic spinel $Co_{0.5}Zn_{0.5}Fe_2O_4$ shows a low band gap E_g = 2.5 eV and after combining with ferroelectric 0.65PT-0.35BNN, further reduction in band gap of **(**1-y)[0.65PT-0.35BNN]-yCZFO composites are observed with increasing the fraction of CZFO. The lowest band gap is E_g = 1.39 eV obtained for y = 0.75 composition as depicted in Fig 3.18(f).

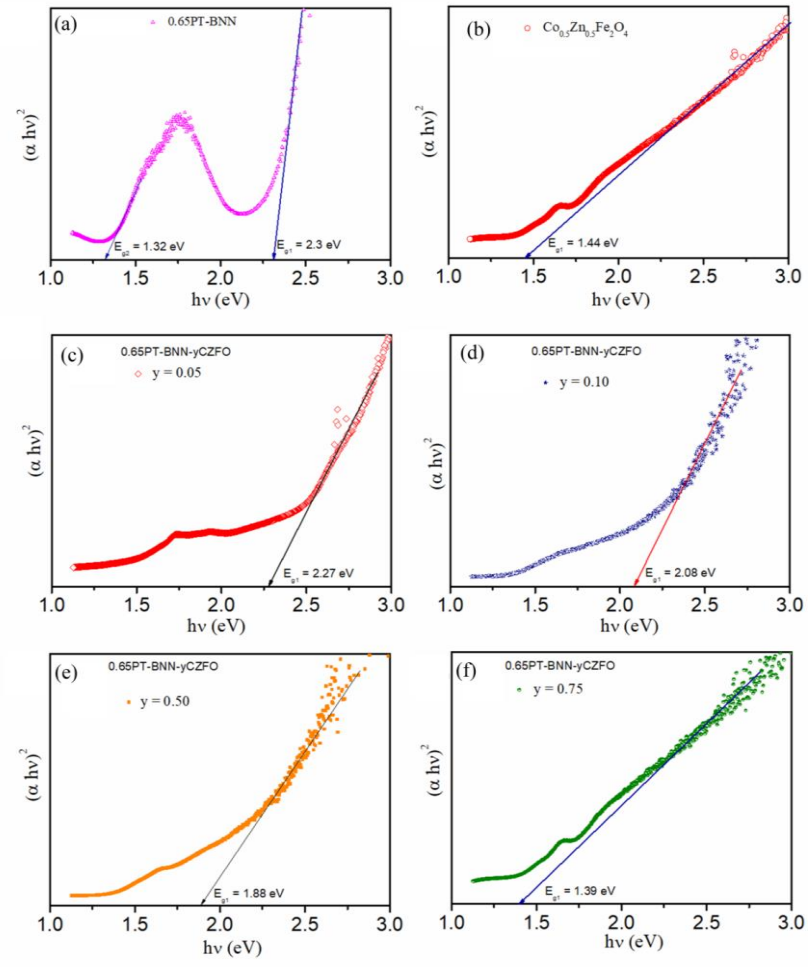

Figure 3.18 Tauc plot $(\alpha h\upsilon)^2$ vs hυ for (a) 0.65PT-0.35BNN, (b) CZFO;and (1-y) [0.65PT-0.35BNN]-yCZFO composites with y = (c) 0.05 (d) 0.10 (e) 0.50 and (f) 0.75.

3.3.7 Band Gap Narrowing and Bulk Photovoltaic Effect in CuO doped $0.65PbTiO_3$-$0.35Bi(Ni_{2/3}Nb_{1/3})O_3$ Ferroelectric Ceramics

In this section of chapter, we report the synthesis of 0.65PT-0.35BNN solid solution with and without CuO doping. Our work is focused on synthesis of low band gap 0.65PT-0.35BNN by CuO doping (PT-BNNC) and find out the bulk photovoltaic effect from as prepared solar cells. The Powder X-ray diffraction patterns of 0.65PT-BNN with and without CuO doping is shown in Fig.3.19. As can be seen from this figure, the 0.65PT-0.35BNN samples have a phase pure perovskite structure at 0.3% CuO doping but very weak CuO diffraction peaks are observed for sample with 1% doping. With CuO addition, the angular shift in XRD peaks is also observed. The optical band gap of CuO doped 0.65PT-0.35BNN is decreased from 2.13eV to 1.8eV as shown in Fig.3.20 (a). This may be due to the presence of sub-bands created by Ni and Cu ions between conduction band and valence band. The oxygen vacancies also play a role to reduce the conduction band position by lowering its tail. It can be concluded that due to strong hybridization between Ni-3d, Cu-3d and O-2p states the band gap of CuO doped 0.65PT-0.35BNN is reduced. A simplified energy band diagram of system is depicted in inset of Fig.3.20 (a) which shows the sub band position formed between conduction band and valence band. There is also second slop in low energy range of Tauc plot and the obtained band gap from that threshold can be termed as E_{g2} which is lower than the main band gap E_{g1} as illustrated in Fig. 3.20 (b). The origin of E_{g1} may be due to p-d charge transfer excitations and E_{g2} is attributed to charge transfer due to O-2p and Ni/Cu-3d excitations

For I-V measurement, the sintered pellets were polished in very thin form. The one side of thin pellet is attached to silicon wafer using silver paste and dried. The ZnO:Al (AZO) thin film is thermally deposited using circular mask which act as top

electrode. Before I-V measurement, the pellets were poled at 100 ^{o}C. The I-V was measured in dark and under green laser light (λ=532 nm) illumination. Fig. 3.21 shows the J-V curves of poled samples in dark and under laser light illumination and inset is showing the schematic diagram of device during measurement. It is observed that 0.65PT-0.35BNN sample shows an open circuit voltage (V_{oc}) ~ 4.13V which increases to 5.1 V for sample with 0.3% CuO doping. The short circuit current density (J_{sc}) increases from 0.19μA/cm^2 to 0.26 μA/cm^2. Further doping of 0.65PT-0.35BNN with 1% CuO slightly reduces its V_{oc}~ 3.9 V but J_{sc}~0.28 μA/cm^2. The increase in photo-current is directly related to reduction in band gap of the material. The observed change in open circuit voltage is related to ferroelectric nature of material which changes with CuO doping [Y. Chang et al. (2017)]. The I-V curve shows slight deviation from linear behaviour which shows the evidence of Schottky contacts between AZO and PT-BNNC surface. The decrease in V_{oc} for 1% CuO doped 0.65PT-0.35BNN can be related to its poor spontaneous polarization.

Fig. 3.22 illustrates the energy band diagram of AZO/PT-BNNC/Ag after positive polarization. Built-in-field which formed at AZO/PT-BNNC and PT-BNNC/Ag interface is termed as E_t and E_b. Depolarization field is termed as E_d which is opposite to polarization P. The net internal electric fields in AZO/PT-BNNC and PT-BNNC/Ag interfaces will be E_t+E_d and E_b-E_d respectively after positive poling. The photo-induced electrons flow towards Ag electrode and holes flow towards AZO electrode, resulting in photo-current. As the direction of net Schottky electric field and depolarization field are in same direction, so net internal built-in potential will be much higher and give higher open circuit voltage.

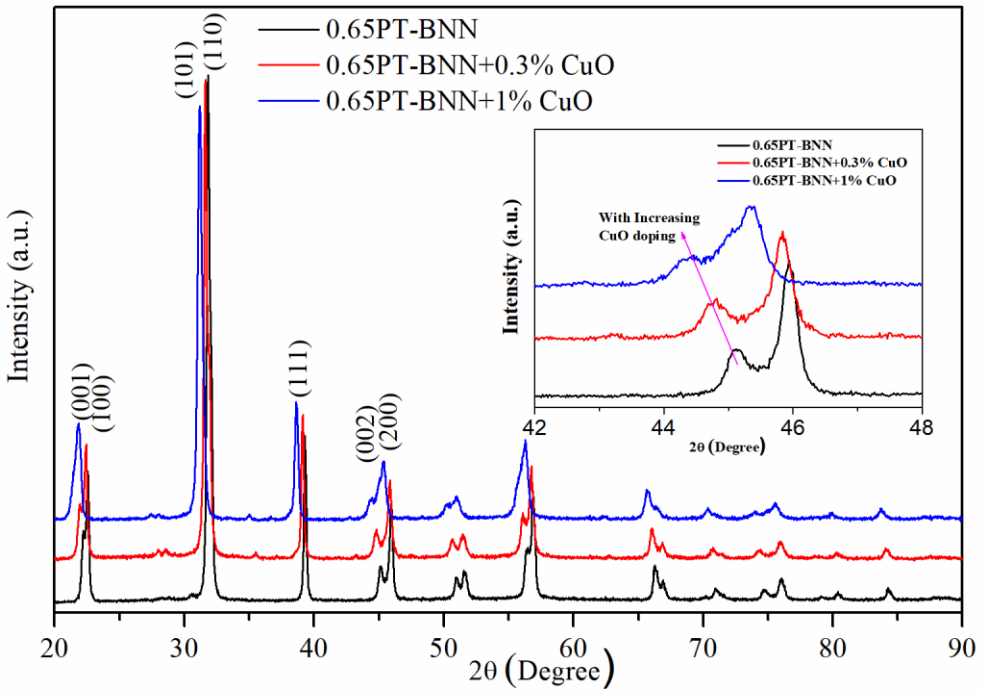

Figure 3.19 Powder X-ray diffraction patterns of 0.65PT-0.35BNN with and without CuO doping. Inset is showing the change in position of x-ray diffraction peak with CuO doping.

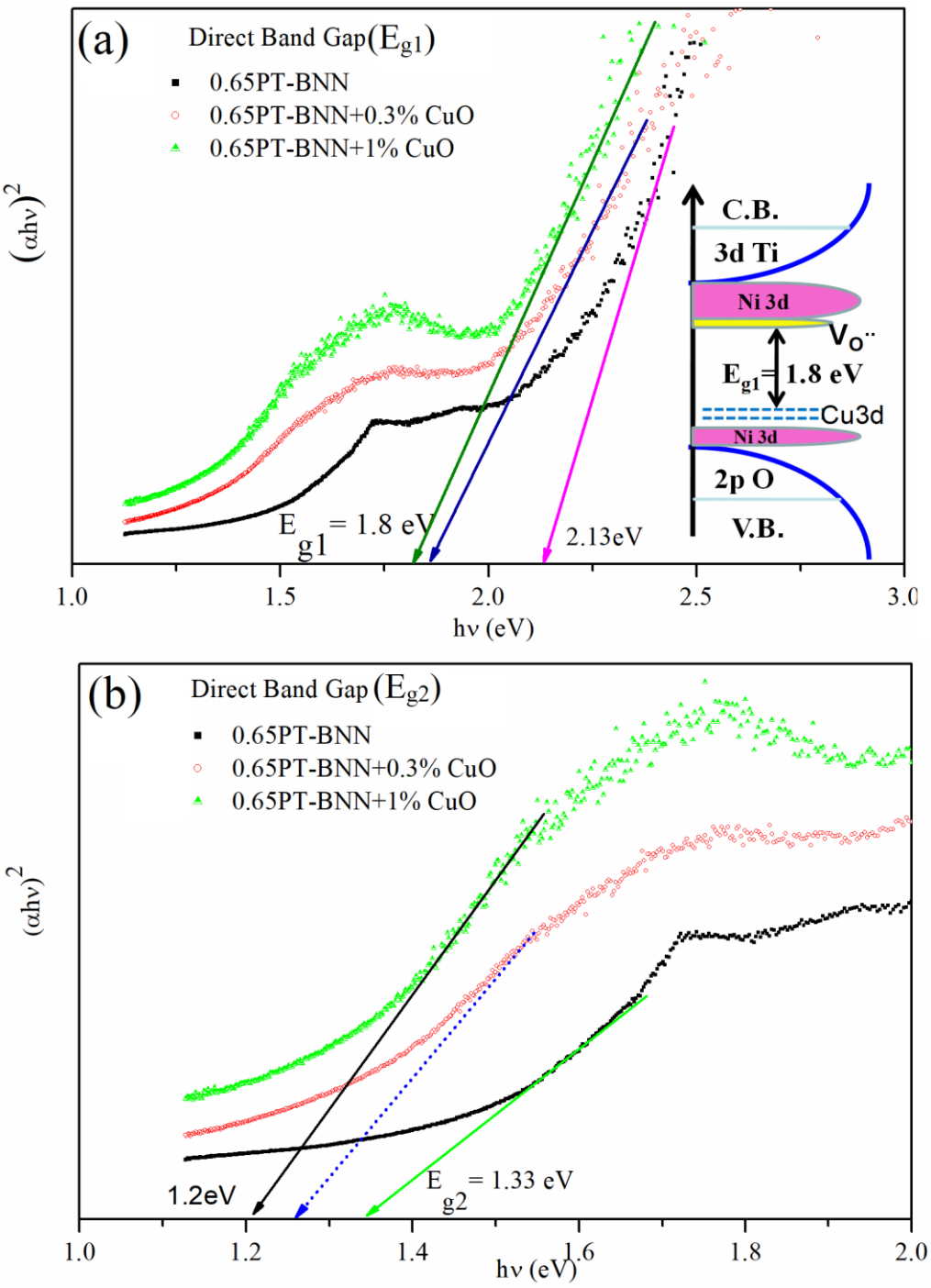

Figure 3.20 The Tauc plot $(\alpha h\upsilon)^2$ vs hυ for 0.65PT-0.35BNN solid solution with and without CuO doping. Two different slopes provide two characteristic threshold band gaps. (a)The first threshold band gap is denoted as E_{g1}. Inset is showing the simplified energy band diagram of system. (b) Second threshold band gap E_{g2}.

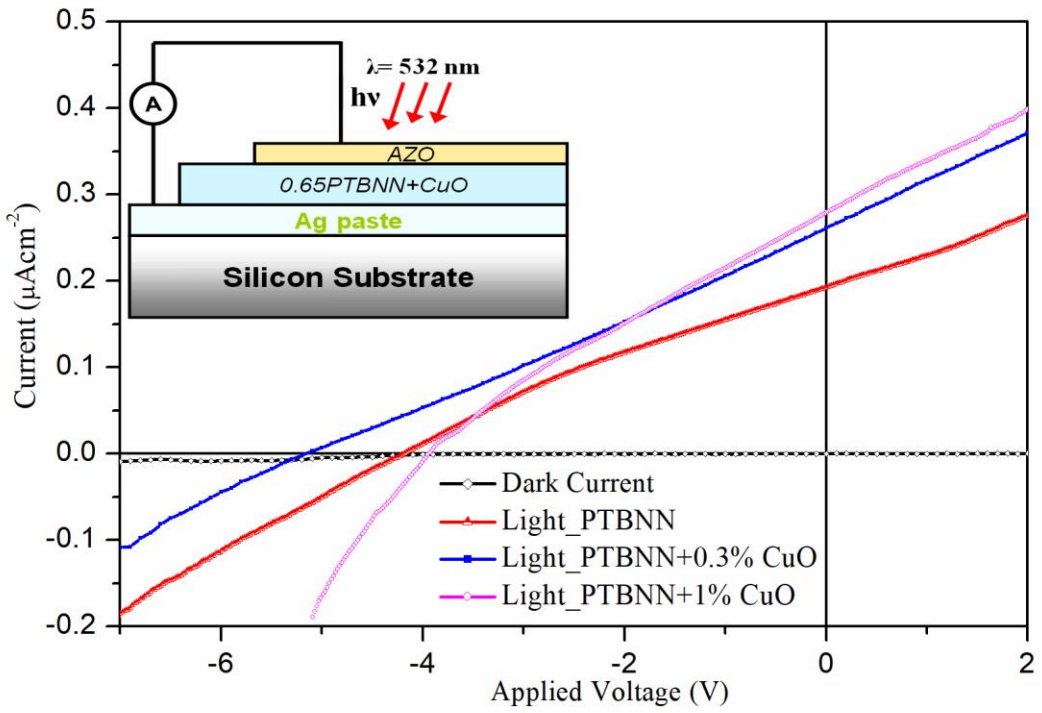

Figure 3.21 Linear J-V Characteristic of Solar cells in dark and under light with Device structure: AZO/0.65PT-BNN-CuO/ /Ag, the inset is schematic design of device.

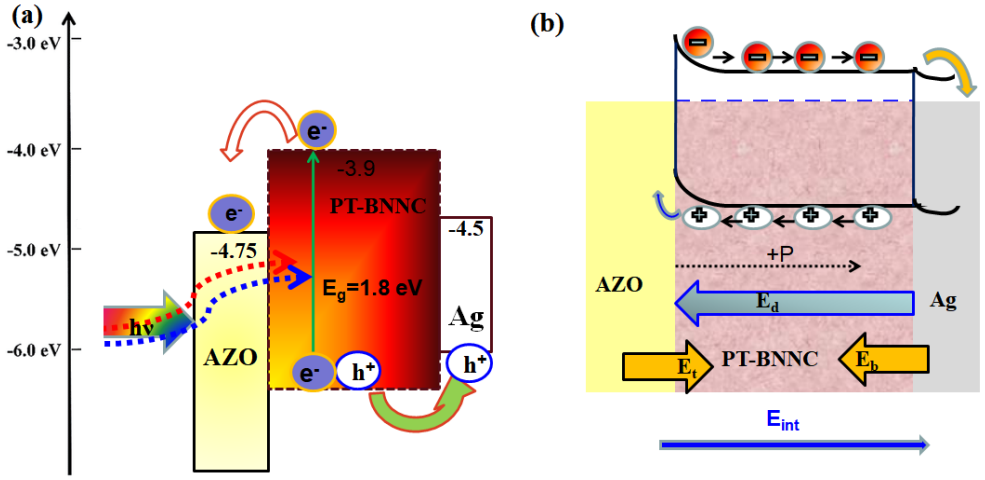

Figure 3.22(a) A schematic energy level diagram for AZO/PT-BNNC/Ag Hetero-structure showing the internal photo-electron generation process (b) Internal electric field distribution showing the dotted arrow which represents the applied polarization direction and big blue arrow shows the depolarization field direction.

3.3.8 Fabrication of PT-BNN Thin Film and study of Nano-scale ferroelectric phenomenon

Apart from the investigation of effect of various dopants in PT-BNN, we also studied the impact of thin film preparation on the behaviour of PT-BNN. The ferroelectric thin films of $0.65PbTiO_3$-$0.35Bi(Ni_{2/3}Nb_{1/3})O_3$(65PTBNNO) were grown on $SrTiO_3$ (001) (STO) single crystal-substrates by pulsed laser deposition (PLD). The ferroelectric 65PTBNNO thin films were deposited at a substrate temperature of 625°C in 0.4 mbar partial pressure of O_2 and Ar. Two films with layer thickness 20 nm and 200 nm were deposited and their surfaces were investigated using atomic force microscopy (AFM). Fig. 3.23(a) shows the AFM topography of 20 nm thin film and Fig. 3.23 (b) shows the AFM topography of 200 nm thin film of 65PTBNNO deposited on STO substrates. From AFM topography investigation, it is found that both types of grown films have smooth surfaces with RMS roughness less than 1.5 nm. We have investigated the ferroelectric domain structure of 65PTBNNO films at nanoscale using combination of atomic force microscopy (AFM) and piezo-response force microscopy (PFM). To characterize the surface of 65PTBNNO films, 5µm x 5µm area of film has been scanned. Fig. 3.24 (a) shows the PFM amplitude mode and Fig. 4.24 (b) shows the PFM phase mode images of 65PTBNN film for 200nm thickness. The resulting contrast confirms the ferroelectricity at nanoscale as the ferroelectric domains are seen clearly. The PFM results confirm the polarization charge in 65PTBNNO film at nanoscale. Varieties of domain structures are observed on PFM phase image which is due to difference in shape and size of grains. The single and multistate-polarization can also be observed. The bright and dark contrasts indicate the down-polarization and up-polarization states in Fig.3.24. The domain walls are clearly observed in PFM amplitude image and marked by arrow in Fig. 3.24 (a).

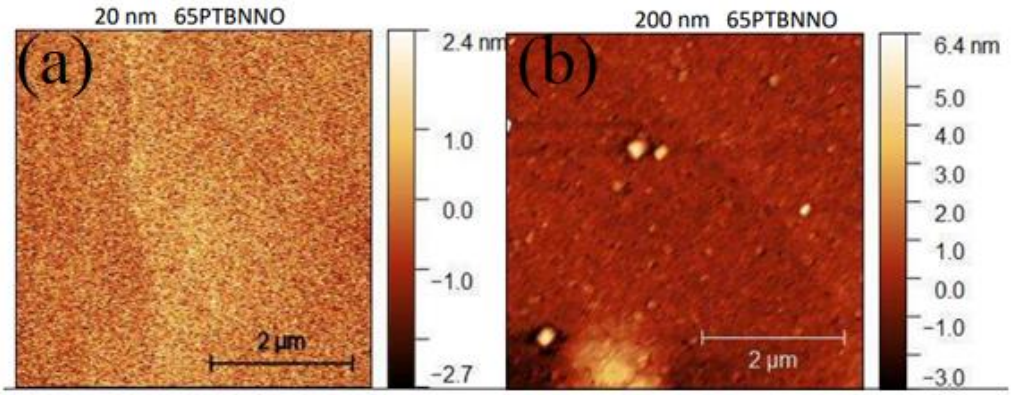

Figure 3.23 AFM topography image of 65PTBNNO thin film with different thickness (a) 20 nm and (b) 200 nm.

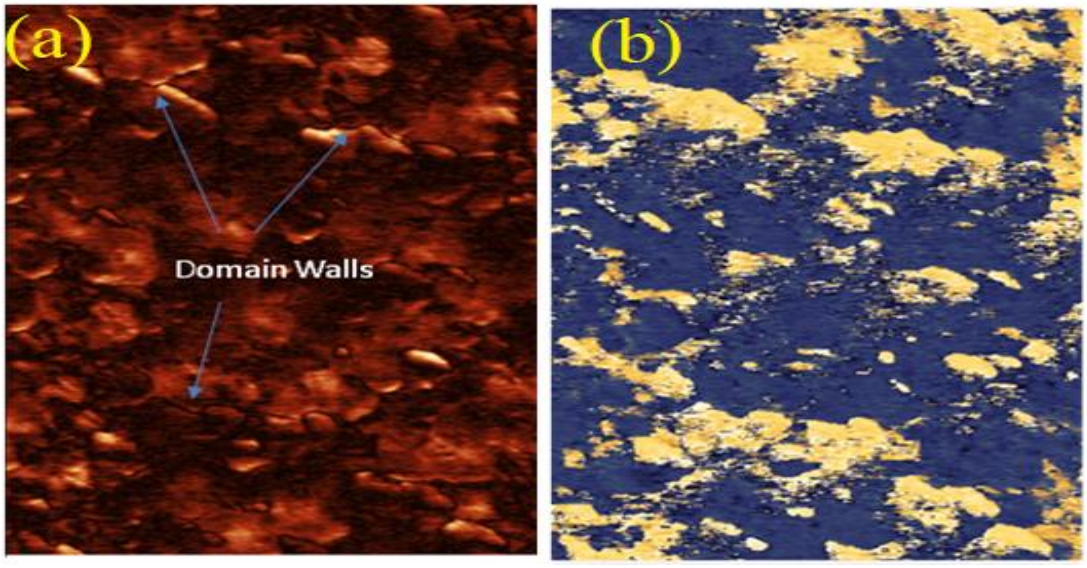

Figure 3.24 (a) PFM Amplitude image (b) PFM Phase image of 65PTBNN thin film. Arrows indicate the domain walls.

3.3.9 Current-Voltage (I-V) Characteristics of AZO/65PTBNNO/LSMO/STO Heterojunction Device

For device fabrication, LSMO bottom electrode has been deposited on STO substrates prior to deposition of ferroelectric thin film. The 10 nm thickness of LSMO in device has been used. The ferroelectric 65PTBNNO thin film was grown on LSMO buffer layer using PLD. For top electrode 100 nm thin ZnO:Al (AZO) film was sputtered on top of 65PTBNNO surface using 100 μm circular mask.The schematic diagram of AZO/65PTBNNO/LSMO/STO heterostructure device is shown in Fig. 3.25. Here, we report the photovoltaic effect for AZO/65PTBNNO/LSMO/STO heterostructure device, where AZO acts as the top transparent electrode and LSMO is the bottom electrode. The current-voltages (I-V) characteristics of as prepared devices were measured by using electrometer in dark and under light illumination. For light illumination, laser (λ = 520 nm) light with power of 15 mW, 20mW and 25 mW were used. Fig. 3.26 shows I-V curves of device in dark and under light illumination. A clear bulk photovoltaic behaviour was seen for the device. From these I-V curves, a short-circuit (I_{sc}) of 0.3 nA and open-circuit voltage (V_{oc}) of 240mV were obtained for the device. When light is illuminated on AZO top side, the electronic charges are generated in the 65PTBNNO layer. The internal electric field in 65PTBNNO layer separates the photo-generated electronic charge carriers. The transportation of electrons and holes gives rise to a photocurrent at zero external bias voltage. It is observed that the photocurrent increases monotonously with lased light power which is due to more generation of electron-hole pairs at higher intensity.

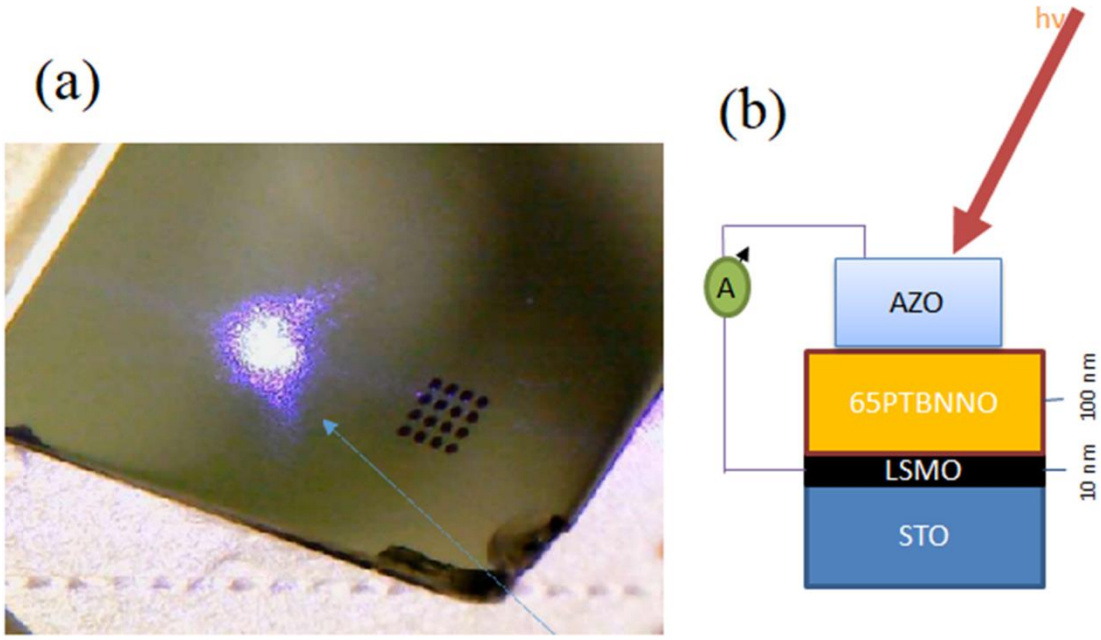

Figure 3.25 Real time measurement image of device during laser light illumination and schematic diagram of AZO/65PTBNNO/LSMO/STO heterojunction device.

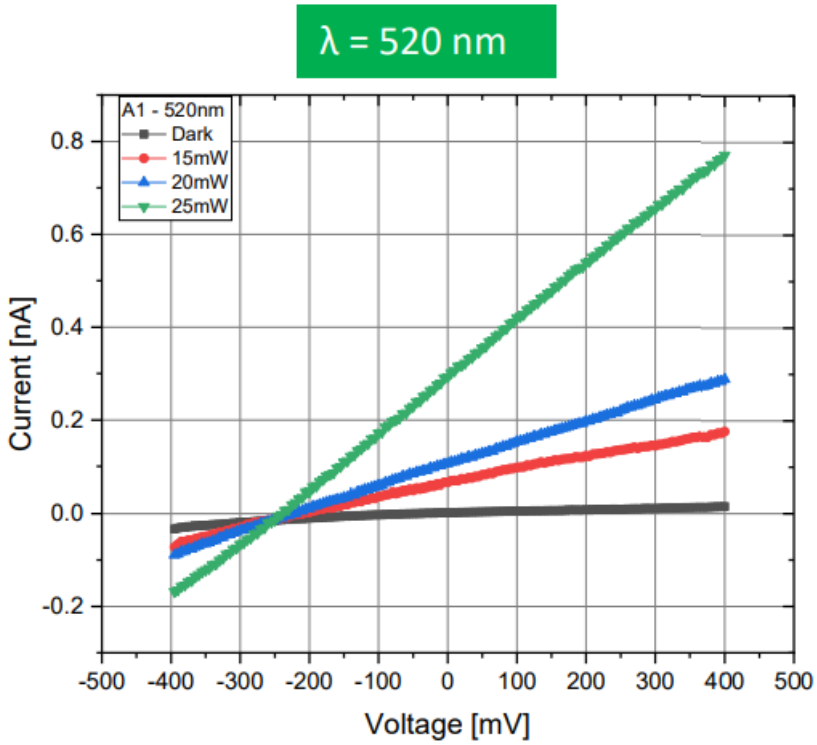

Figure 3.26 I-V characteristics of AZO/65PTBNNO/LSMO/STO heterojunctionin dark and under 520 nm laser light illumination.

3.4 Conclusions

In this chapter, $xPbTiO_3$-(1-x)$Bi(Ni_{2/3}Nb_{1/3})O_3$ solid solution with compositions (x= 0.87, 0.77, 0.70, 0.67, 0.66, 0.65, 0.64, 0.63, 0.625, 0.62, 0.60, 0.55 and 0.50) were successfully prepared by solid state ceramic synthesis and characterized for crystal structure and optical properties. PT-BNN shows the MPB region in the composition range of x = 0.65 to x =0.60, where tetragonal and rhombohedral phases coexist. The crystal structure transitions as a function of composition in PT-BNN has been confirmed by Raman spectroscopy analysis. Composition dependent dielectric properties are also studied. MBP region composition 0.65PT-0.35BNN shows the highest value of dielectric permittivity and remnant polarization (P_r = 25.6 μC/cm^2) and a direct band gap E_g = 2.3 eV. The band gap is significantly reduced for $Bi(Ni_{2/3}Nb_{1/3})O_3$doping in $PbTiO_3$. This work provides good insights for the band gap tuning of $PbTiO_3$ with varying the concentration of $Bi(Ni_{2/3}Nb_{1/3})O_3$. The band gap of material is directly influenced by transition elements (Ni, Co, Cu) doping and changing the stoichiometric ratio of Ni and Nb in $Bi(Ni_{2/3}Nb_{1/3})O_3$. The Co-doping in 0.65PT-0.35BNN provide the lowest band gap (E_g = 1.55 eV) but ferroelectric polarization is also decreased. The multiferroic particulate composites of spinel NZFO and CZFO and 0.65PT-0.35BNN also effectively provide a low band gap. In Table 3.2, the experimentally obtained band gap in this chapter is compared with previously reported band gap of perovskite oxides. The bulk photo-voltaic effect is analyzed in CuO doped 0.65PT-0.35BNN ceramic pellets. The photovoltaic behaviour is also observed in 0.65PT-0.35BNN thin films deposited by PLD. Thus, we can conclude that PT-BNN ceramic is an excellent photovoltaic material for thin film solar cells.

Table 3.2: Comparative Band gap

Serial No	Composition (In This Work)	Band gap eV(Direct)	Composition (In literature)	Band gap eV	Reference
1	$PbTiO_3$	2.8	$PbTiO_3$	3.2	T. Zheng et al. (2016)
2	$0.87PbTiO_3$-$0.13Bi(Ni_{2/3}Nb_{1/3})O_3$ (0.87PT-BNN)	2.41			In this work
3	0.77PT-BNN	2.40			In this work
4	0.70PT-BNN	2.27			In this work
5	0.65PT-BNN	2.32	0.65PT-BNN	3.0	H. Liu et al. (2015)
6	0.63PT-BNN	2.41			In this work
7	0.60PT-BNN	2.44			In this work
8	0.55PT-BNN	2.48			In this work
9	$0.65PbTiO_3$-$0.35Bi(Ni_{2/3+0.07}Nb_{1/3-0.07})O_3$	2.23			In this work
10	$0.65PbTiO_3$-$0.35Bi(Ni_{1/3}Co_{1/3}Nb_{1/3})O_3$	1.55			In this work
11	$0.58PbTiO_3$-0.42 $Bi(Co_{2/3}Nb_{1/3})O_3$	1.3			In this work
12	$0.65PbTiO_3$-$0.35Bi(Ni_{1/3}Cu_{1/3}Nb_{1/3})O_3$	1.8			In this work
13	0.90(0.65PTBNN)-0.10NZFO	1.56			In this work
14	0.25(0.65PTBNN)-0.75CZFO	1.39			In this work
15			$0.62PbTiO_3$-$Bi(Ni_{2/3}Ta_{1/3})O_3$	1.85	D. Pang et al. (2018)
16			$Pb(Zr,Ti)O_3$	3.6	A. Perez-Tomas et al. (2018)
17			$BaTiO_3$	3.3	C. Paillard et al. (2016)
18			$LiNbO_3$	3.78	A. Dhar et al. (1990)
19			$BiFeO_3$	2.7	SR Basu et al. (2008)
20			$Bi(Fe_{1-x}Co_xO)_3$	2.3	AK Sinha (2021)
21			$Ba_{1-x}(Bi_{0.5}Li_{0.5)x}TiO_3$	3.2	S. Pal et al. (2018)
22			$BaTi_{0.925}(Mn_{1/2}Nb_{1/2})$	1.66	S. Das et al. (2018)
23			$BaTi_{0.93}Sn_{0.07}O_3$	2.61	L. Kola et al. (2019)
24			$Bi_4NdTi_3FeO_{15}$	2.54	L. Cao et al. (2019)
25			$Pb(Ti_{0.85}Ni_{0.15})O_{3-\delta}$	2.67	W. Zhou et al. (2016)